THE GROWTH OF SNSBSE2 CRYSTAL AND THE INVESTIGATION OF PHYSICAL PROPERTIES OF THERMALLY EVAPORATED SNSBSE2 THIN FILMS

A THESIS SUBMITTED TO
THE GRADUATE SCHOOL OF NATURAL AND APPLIED SCIENCES
OF
MIDDLE EAST TECHNICAL UNIVERSITY

BY

TUNÇ BEKTAŞ

IN PARTIAL FULFILLMENT OF THE REQUIREMENTS
FOR
THE DEGREE OF MASTER OF SCIENCE
IN
PHYSICS

FEBRUARY 2022

Approval of the thesis:

THE GROWTH OF SNSBSE2 CRYSTAL AND THE INVESTIGATION OF PHYSICAL PROPERTIES OF THERMALLY EVAPORATED SNSBSE2 THIN FILMS

submitted by **TUNÇ BEKTAŞ** in partial fulfillment of the requirements for the degree of **Master of Science in Physics Department, Middle East Technical University** by,

Prof. Dr. Halil Kalıpçılar
Dean, Graduate School of **Natural and Applied Sciences**

Prof. Dr. Seçkin Kürkcüoğlu
Head of Department, **Physics**

Prof. Dr. Mehmet Parlak
Supervisor, **Physics, METU**

Prof. Dr. Çiğdem Erçelebi
Co-supervisor, **Physics, METU**

Examining Committee Members:

Prof. Dr. Çiğdem Erçelebi
Physics Dept., METU

Prof. Dr. Mehmet Parlak
Physics Dept., METU

Assoc. Prof. Dr. Özge Sürücü
Electics and Electronics Enginnering Dept., Atilim University

Assoc. Prof. Dr. Emre Yüce
Physics Dept., METU

Assoc. Prof. Dr. Tahir Çolakoğlu
Physics Engineering Dept., Ankara University

Date: 02.02.2022

I hereby declare that all information in this document has been obtained and presented in accordance with academic rules and ethical conduct. I also declare that, as required by these rules and conduct, I have fully cited and referenced all material and results that are not original to this work.

Name, Surname: Tunç Bektaş

Signature :

ABSTRACT

THE GROWTH OF SNSBSE2 CRYSTAL AND THE INVESTIGATION OF PHYSICAL PROPERTIES OF THERMALLY EVAPORATED SNSBSE2 THIN FILMS

Bektaş, Tunç
M.S., Department of Physics
Supervisor: Prof. Dr. Mehmet Parlak
Co-Supervisor: Prof. Dr. Çiğdem Erçelebi

February 2022, 70 pages

The aim of this study is to characterize the structural, optical and electrical properties of both SnSbSe bulk crystal and SnSbSe thin films. For this purpose, SnSbSe crystal were grown and SnSbSe thin film were deposited on glass substrates by using vertical Bridgman and thermal evaporation methods respectively. For SnSbSe bulk crystal, Energy Dispersive X-Ray, Scanning Electron Microscopy, X-Ray Diffraction and Raman measurement were performed to investigate the structural analysis. Also, spectroscopic ellipsometry measurement carried out to obtain index of refraction, extinction coefficient and optical band gap for optical characterization. The *I*-*V* measurement of a crystal also performed in dark and illuminated manner for electrical characterization. To examine the effect of annealing on the physical properties of SnSbSe thin films, samples were annealed at 100 °C, 200 °C, 300 °C and 400 °C for 30 minutes and one of the samples kept as 'as grown'. The structural properties of these samples were analyzed by Energy Dispersive X-Ray, Scanning Electron Microscopy, X-Ray Diffraction, Raman and Atomic Force Microscopy analysis. For the optical caharacterization, UV-Vis spectroscopy measurement carried out for obtaining absorption coeeficients and the optical band gap of samples and observing the effect of annealing on band gap. For the electrical characterization, the temperature dependent photoconductivity measurement performed for measuring the conductivities and activation energies of samples.

Keywords: SnSbSe, Bridgman growth, thermal evaporation, structural, optical and electrical characterization

ÖZ

SNSBSE2 KRİSTALİ BÜYÜTÜLMESİ VE ISIL BUHARLAŞTIRMA YÖNTEMİ İLE KAPLANAN SNSBSE2 İNCE FİLMLERİN FİZİKSEL ÖZELLİKLERİNİN İNCELENMESİ

Bektaş, Tunç
Yüksek Lisans, Fizik Bölümü
Tez Yöneticisi: Prof. Dr. Mehmet Parlak
Ortak Tez Yöneticisi: Prof. Dr. Çiğdem Erçelebi

Şubat 2022 , 70 sayfa

Bu çalışma SnSbSe kristal yapısının ve SnSbSe ince filmlerin yapısal, optik ve elektriksel özelliklerini karakterize etmeyi amaçlamaktadır. Bu amaç doğrultusunda SnSbSe kristal yapısı dikey Bridgman yöntemiyle, SnSbSe ince filmler ise cam alttaş üzerine ısıl buharlaştırma yöntemiyle büyütülmüştür. SnSbSe kristalinin yapısal özellikleri, enerji dağılım X-ışını, taramalı elektron mikroskopi, X-ışını kırınımı ve Raman spektroskopi yöntemleriyle analiz edilmiştir. Ayrıca, malzemenin optik özellikleri elipsometri yöntemiyle incelenerek kırıcılık indisi, sönüm katsayısı ve yasak enerji bant aralığı elde edilmiştir. Söz konusu kristalin iletkenliğini ve bu iletkenliğin ışığa olan tepkisini incelemek amacıyla karanlık ortamda ve ışık altında akım-voltaj ölçümü yapılmıştır. Farklı tavlama sıcaklıklarının SnSbSe ince filmlerin fiziksel özelliklerine olan etkisini incelemek amacıyla ince filmler 100 °C, 200 °C, 300 °C and 400 °C sıcaklıklarda 30 dakika süreyle tavlanmıştır. Söz konusu ince film örneklerin yapısal özellikleri enerji dağılım X-ışını, taramalı elektron mikroskopi, X-ışını kırınımı, Raman spektroskopi ve atomik kuvvet mikroskopi yöntemleriyle analiz edilmiştir.

SnSbSe ince filmlerin optik özellikleri Ultraviole-Görünür ışık spektoskopi yöntemiyle karakterize edilmiş, örneklerin soğurma katsayıları, yasak enerji bant aralıklar ve farklı tavlama sıcaklıklarının bant aralığına olan etkisi değerlendirilmiştir. SnSbSe ince filmlerin iletkenlikleri ve aktivasyon enerjileri sıcaklık bağımlı ışık-kondüktivite ölçümleri sonucunda hesaplanmıştır.

Anahtar Kelimeler: SnSbSe, Bridgman, ısıl buharlaştırma, ince film, karakterizasyon

Dedicated to Dr.Vedat Tanrıverdi

ACKNOWLEDGMENTS

First of all, I would like to thank to my supervisor Prof. Dr. Mehmet Parlak for his guidance. He is always gentle, genial, patient, supportive and it is a pleasure to study under his supervision. Furthermore, the contributions of my co-supervisor Prof. Dr. Ayşe Çiğdem Erçelebi are kindly acknowledged.

I am greatful to Dr. Makbule Terlemezoğlu and Assoc. Prof. Dr. Özge Sürücü for their guidance and valuable suggestions. They always share their scientific knowledge and experiences with me and encourage me to do better. I am also greatful to Assoc. Prof. Dr. Gökhan Sürücü for his helpful comments and supportive conversations. Moreover, my lab-mates Assoc. Prof. Dr. Emre Coşkun, Assoc. Prof. Dr. Hasan Hüseyün Güllü, PhD. candidates Çiğdem Doğru Balbaşı and Merve Demir deserve thanks for their contributions.

Also, I offer my deep respects and special thanks to Dr. Vedat Tanrıverdi, PhD. candidates Mussa Rajamov and Sedat Pala for their helpful discussions. Their hard works and dedications give me motivation and inspiration.

Moreover, my dear friends Hasan Canar, Tarek Elsebaei, Giray Mecit, Asım Doğan Namlı, Okan Kurt and PhD. candidates Gence Bektaş, Çiya Aydoğan and Yasin Altun are acknowledged for their supports.

The special thanks go to my family. I always feel the supports of my parents and my fiancee Kadriye Yılmaz. I am greatful to their endless love and supports.

Lastly, I am thankful to The Scientific and Technological Research Council of Turkey (TUBITAK) for funding this research under the project number Tubitak-120F286.

TABLE OF CONTENTS

CHAPTERS

LIST OF TABLES

TABLES

LIST OF FIGURES

FIGURES

LIST OF ABBREVIATIONS

EDX	Energy Dispersive X-Ray Spectroscopy
SEM	Scanning Electron Microscopy
XRD	X-Ray Diffraction
AFM	Atomic Force Microscopy
ICDD	International Center for Diffraction Data

CHAPTER 1

INTRODUCTION

The energy demand is significantly increasing as a result of the population growth and devoloping industrial activities [1]. The energy demand has been met from the sources such as coal and fossil fuels until past few decades. Since these sources lead to air pollution, carbon emission and greenhouse effect, it is inevitable to replace them with sustainable and environment-friendly resources [2]. This motivates the researchers to focus on renewable energy. Among the renewable energy sources such as solar, wind and geothermal; solar energy appears as a promising alternative because of its low cost and high efficiency [3]. Approximately 1000 W/m^2 solar irreadiance reaches surface of the earth [4]. This is huge amount of energy to meet the increasing energy demand. To benefit from this energy, it is necessary to know how to convert the solar energy to electricity. There are couple of ways to benefit from solar energy such as using thermoelectric materials which convert the heat to electricity depending on Seebeck effect, solar thermal collectors which absorb the heat and keep it as a thermal energy and solar cells which convert the incoming sunlight to electricty [5, 6, 7].

The working mechanism of a solar cell depends on photovoltaic effect. Photovoltaic effect was discovered by Edmond Becquerel in 1839 [8] . After the Becquerel's discovery of photovoltaic effect, Willoughby Smith, W.G. Adams and R.E. Day discovered the sensitivity of selenium to light [9]. These discoveries account for the base of solar cell studies. Then, the first solar cell containing amorphous selenium wafers was designed by Charles Fritts in 1883 and the efficiency of this solar cell was only 1 % [10] . After the physics behind the p-n junction was understood, single-crystal silicon wafers started to be used in solar cell production. This wafer based silicon solar cells named as first generation solar cells [11]. In the first generation, the efficiency may reach approximately 18 % and 13 % for single-crystalline and polycrystalline wafers respectively [11]. Then, as a result of the efforts to produce solar cells for industrial purposes, thin film solar cells appears. The thin film solar cells are named as second generation solar cells. In the second generation, amorphous silicon, cadmium telluride and copper indium gallium di-selenide thin layers are used as an absorber layer and their efficiencies are 5-6 %, 9-13 %, 10-12 % respectively [11, 12, 13]. There are also third generation solar cells which are polymer based, perovskite based, nanocrystal based etc. Each of these solar cells have some advantages and disadvantages besides their different purposes of usage.

Before going deep into the thin film solar cells, it is helpful to explain what the thin film is. Thin film is basically a thin layer whose thickness is smaller than the micrometer order. Since it is too thin to hold, thin films are grown on glass, metal, plastic or wafer substrates. There are various thin film growth techniques such as thermal evaporation, e-beam evaporation, sputtering, molecular beam epitaxy, laser ablation etc. The growth technique may differ with respect to the coated material. Furthermore, some growth techniques supply ease of production while some others supply low cost. Thin film is one of the main study areas of solid state physics.

Thin film solar cells are second generation solar cells. Although this type of solar cells are less efficient than the first generation, they have more applications. There is no busbar and finger in thin film solar cells. Also, unlike wafers, it is possible to grow thin film absorber layers on large areas such as windows or building elevations [14]. Furthermore, thin layers can be coated on flexible substrates. Thus, these thin layers are applicable for flexible devices [15]. Chopra et.al. point out that the cost of thin film solar cell production significantly decrases and the capacity of manufacturing increases as the time progressed so that thin film solar cells are becoming a widespread and cheaper alternative [16].

As it is roughly mentioned above, thin film solar cells are made up of silicon (Si), cadmium telluride (CdTe), cadmium sulfide/selenide (CdS/Se) and copper indium gallium di-selenide (CIGS) thin absorption layers [17, 18, 19]. Also, galium arsenide (GaAs) and copper zinc tin sulfide/selenide (CZTS/Se) thin films are possible absorption layers [20, 21]. Despite some advantages, these materials suffer from some disadvantages and limitations. For instance, silicon is an earth-abundant material which supplies ease of production with low cost [22]. However, the light conversion efficiency of amorphous silicon is very poor (around 10 %) [23]. The maximum theoretical efficiency of crystalline silicon solar cells is 29 % while the maximum reached efficiency is around 25 % [24]. These results indicate that if the researchers succeed to overcome the limitations, silicon solar cells are close to reach their maximum theoretical efficiency. Moreover, the usages of either cadmium based (CdTe,CdSe) or Ga-In based (GaAs, InP, CIGS etc.) absorber layers are limited due to the toxicity of Cd and non-abundancies of Ga and In elements [25, 26]. Because of these limitations, researchers are conducted to investigate more abundant, less toxic and low-cost alternative materials. At this point, Sn and Sb based materials such as SnSe and SbSe gain importance due to their cheapness, relatively less toxicity and abundancy.

SnSe, which is one of the transition metal chalcogenides, is a promising material for photovoltaic, optoelectronic and thermoelectric applications [27]. Also, it is used as a memory switch in electronics and as an anode in lithium-ion batteries [28, 29]. SnSe could have p-type and n-type conductivity and it has 1.3 eV direct and 0.9 eV indirect energy band gaps [30, 31]. The crystal structure of SnSe is orthorhombic [31]. SbSe has also solar cell, optoelectronic device, thermoelectric device and IR spectroscopy applications with 1.22 eV direct and 1.21 eV indirect energy band gap [32, 33]. This study focuses on not only the growth of SnSbSe crystal but also the deposition of SnSbSe thin films for optimizing the physical properties of SnSe and SbSe structures.

CHAPTER 2

THEORETICAL CONSIDERATIONS

2.1 Introduction

In this chapter, general knowledge about semiconductors is given. The crystal structure and lattice structures are introduced. Then, the band theory is roughly investigated by explaining formation of bands. The function of bands in conduction mechanism of solids are discussed. Moreover, the most basic application of semiconductors, a p-n junction, is introduced. Finally, the techniques of either crystal growth and thin film deposition or structural, optical and electrical characterization are analyzed.

2.2 Physics of Semiconductors

2.2.1 Crystal Structure

It is possible to categorize solids as crystalline or amorphous. Unlike amorphous solids, atoms are regularly arranged in crystalline structure. Moreover, this regular arrangement repeats itself. The smallest repeating structure is called unit cell [34]. In order to describe the positions of atoms, it is required to define a lattice which consists of many unit cells. The lattice may have different shapes such as cubic, tetragonal or orthorhombic.

2.2.2 Electronic Band Structure

Electrons in an atom stay on some specific discrete energy levels. Solid structures are composed of billions of atoms and these atoms are really close to each other. Hence, the energy levels of electrons are close as well. In such a system, the electrons of an atom and the electrons of its neighbour atom are possibly being at the same energy level. However, Pauli exclusion principle states that it is possible to find only two electrons with different spins in the same energy level [35]. It means that the electrons of neighbouring atoms couldn't be found in the same energy level. Hence, when *N* number of atoms are being together, the exclusion principle results in splitting of an energy level into *N* different energy levels [35]. The energy levels of each electrons in solid structure form the energy bands.

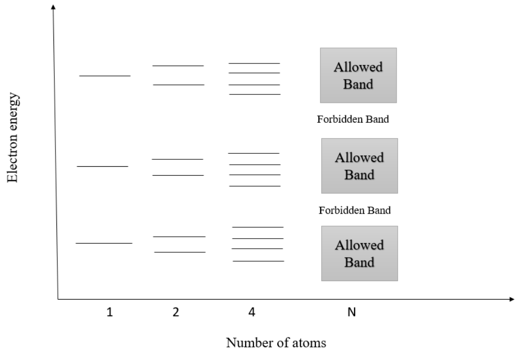

Figure 2.1: The band formation and allowed - forbidden bands

The energy band which is filled at zero degree Kelvin is called the valence band and its nearest allowed energy band is called the conduction band [35]. There is an energy difference between the top of valence band and the bottom of conduction band. This difference is called a band gap. Thus, the energy diagram of a semiconductor is basically modeled as a valence band, conduction band and a forbidden energy gap in between conduction and valence bands. In intrinsic semiconductors, the valence band is totally full whereas the conduction band is empty at low temperatures.

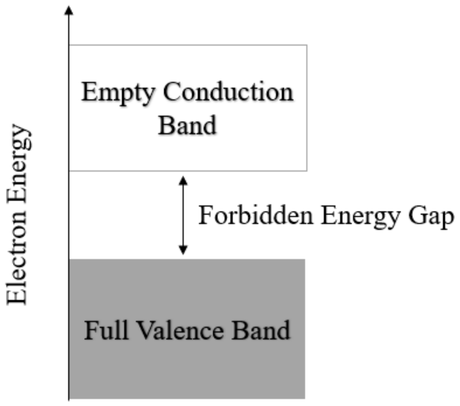

Figure 2.2: The bands of a semiconductor at low temperatures

If a semiconductor is illuminated by light whose energy is less than the energy band gap of semiconductor, the incident photon couldn't be absorbed. The semiconductor behaves like a transparent material and the incident light just passes through it [36]. If the energy of the incident light is greater than the energy band gap of semiconductor, the photon is absorbed and electron-hole pair is created as a result of the transition of electron from valence band to the conduction band. There are two band to band transition mechanisms named as direct and indirect transitions.

The energy vs wavevector (E vs k) diagrams are given in the figures 2.3 and 2.4. In direct transition, the maxima of valence band and the minima of conduction band has the same k value which is k = 0. In semiconductors which have direct band gap, the energy of photon emitted by electron-hole recombination is equal to the band gap energy. Therefore, energy is conserved. However, the k values of the maxima of valence band and the minima of conduction band are different in indirect transition. Therefore, the momentum conservation is required for transition. This momentum requirement is supplied by phonons which exist in lattice due to lattice vibration [37]. If no phonons exist (i.e at low temperatures), no band transition takes place even if the energy of incident photon is greater than band gap energy.

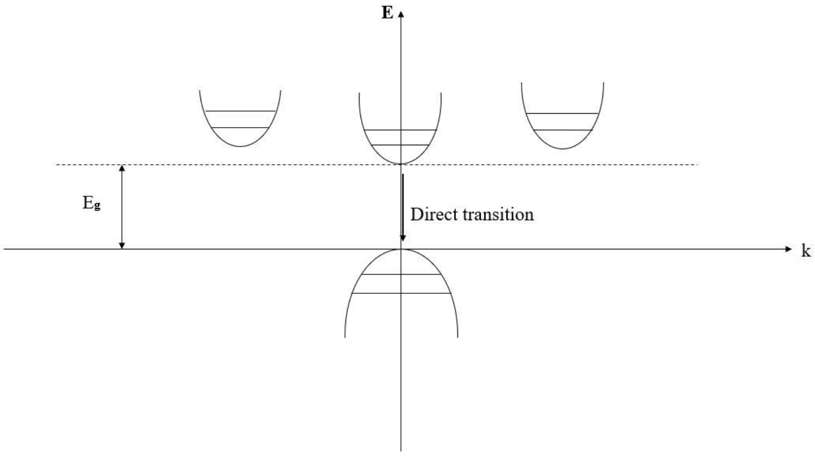

Figure 2.3: The direct band to band transition

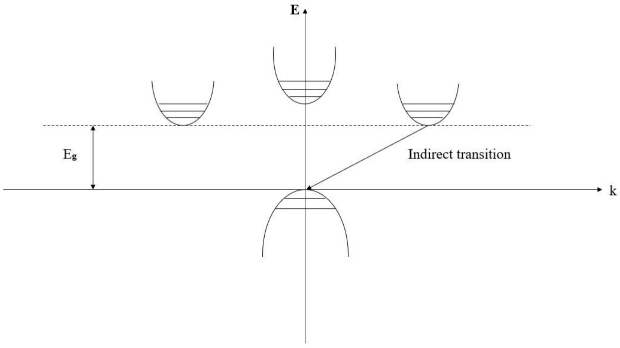

Figure 2.4: The indirect band to band transition

2.2.3 P-N Junction

When the energy whose amount is greater than the energy band gap is given to the electrons in valence band, these electrons are excited and jump to the conduction band. Thus, the excited electrons contribute to the electrical conduction. Electrons are negative charge carriers. When the electron in valence band jump to the conduction band, it leaves a vacant position in valence band. The vacancy can be considered as a positive charge carrier. This positive charqe carrier is named as a hole. The number of electrons in conduction band and the number of holes in valence band are equal for intrinsic semiconductors. The number of positive and negative charge carriers can be increased by doping additional atoms, in this case, the semiconductor is named as extrinsic semiconductor. In extrinsic semiconductors, major charge carriers determine the type of conductivity such that the semiconductor has p-type conductivity if the major charge carriers are holes and it has n-type conductivity if the major charge carriers are electrons. The joining of p-type and n-type materials creates a p-n junction which is one of the most basic semiconductor devices. Light sensitive diodes, variable capacitance diodes and light emiting diodes, laser diodes and switching diodes are some applications of p-n junction [35].

2.3 Crystal Growth Techniques

2.3.1 Bridgman Growth

The Bridgman or Bridgman-Stockbarger method is a way to grow both single crystals and polycrystals. In this method, crystallization takes place in a furnace including temperature zones. It is helpful to denote these zones as high temperature and low temperature zones. There is also another zone between these two zones. The high temperature zone is hotter and the low temperature zone is colder than the melting point of precursors (sources i.e. powder, pellet etc.). Therefore, there is a heat flux in a furnace [38]. In this technique, the crucible moves in the direction of heat flux. Thus, the precursors which melt in high temperature zone solidfy in the low temperature zone. This solidification yields a crystal structure. The temperature difference of zones creates a temperature gradient in a furnace. In Czochralski growth technique, the melt/seed interface is fixed, heat transfer and pulling velocity determine the radius of grown crystal [39]. In Bridgman growth technique, the grown crystal and the crucible has the same radius, and heat transfer determines the melt/seed interface [Bridgmann.pdf]. At the interface, thermal stress is minimized, so there are less dislocations. This is the advantageous of Bridgman growth. The Bridgman growth in both vertical and horizontal furnaces are possible.

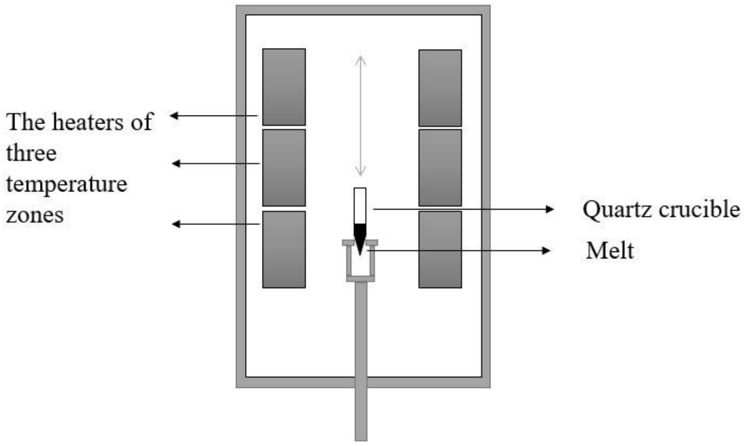

Figure 2.5: The schematic representation of vertical Bridgman system

2.4 Thin Film Deposition Techniques

Thin film deposition techniques have a wide spectrum. There are physical, chemical and plasma based deposition techniques such as electron beam evaporation, chemical vapor deposition and sputtering. Some of these techniques supply low-cost and ease of fabrication. Also, the characteristic properties (melting temperature etc.) of deposited material determines the growth technique.

2.4.1 Physical Vapour Deposition

In physical vapour deposition method, the source element is vaporized in a vacuum environment. Then, the vapour is carried up to a substrate and it becomes condensed on the substrate. The source element can be evaporated by heating, sputtering or bombarding with electron beam. Depending on the vaporization method, PVD tecniques get different names such as thermal evaporation, e-beam evaporation, laser ablation, cathodic arc deposition.

2.4.1.1 Thermal Evaporation

Thermal evaporation is one of the PVD method in which the source material is evaporated by heating in high vacuum about 10^{-6} or 10^{-7} Torr order. This method is preferable because of its ease of fabrication. In thermal evaporation, there is a thermal boat including source materials, substrates, the probe of thickness monitor and a shutter in a vacuum chamber. After the air in chamber is evacuated by a vacuum pump, the boat is heated up to the evaporation temperature of material. Then, the shutter is removed to allow the vapour to move through the substrate. The temperature must be increased slowly in order to keep the rate of evaporation as low as possible for controllable deposition.

2.5 Characterization Methods

In this part, some of the structural, optical and electrical characterization techniques are introduced.

2.5.1 Structural Characterization Methods

In order to characterize the structure of a material, there are several methods such as X-Ray Diffraction (XRD), Scanning Electron Microscopy (SEM), Energy Dispersive X-Ray Analysis (EDAX) and Atomic Force Microscopy (AFM). These methods supply various information about the material's structure. For instance, XRD allows to calculate lattice parameters such as strees, strain, interplanar distance and dislocation density. SEM gives the detailed image of the surface to observe the grains, cracks or any contaminations on the surface. EDAX analysis provides the atomic ratios of atoms that exist in structure and AFM allows to analyze the morpholgy of the structure.

2.5.1.1 X-Ray Diffraction (XRD)

Solids may exist in amorphous and crystalline form. Crystal is a structure in which the atoms are located in a pattern and this pattern repeats itself periodically. X-Ray Diffraction (XRD) is a simple way to analyze the crystal structure. It supplies the orientation of crystal structure. In XRD, the X-Ray beam (λ = 1.54 Å) is sent to the sample with an angle and the beam is scattered from the surface and detected by a detector. The incident and diffracted beams have the same angle with normal as it is seen in figure 2.8. Due to the design of X-Ray spectrometer, an angle between the incident and diffracted light is 2. The X-Ray Diffraction is formulated by Bragg's law [40].

$$n\lambda = 2dsin\theta \tag{2.1}$$

Hence, the interatomic distance (d) is given as

$$d = \frac{n\lambda}{2sin\theta} \tag{2.2}$$

For the first order diffraction (n=1),

$$sin\theta = \frac{\lambda}{2d} \tag{2.3}$$

Since sinθ can take the values between -1 and +1, sin$\theta \leq 1$.

Thus,

$$sin\theta = \frac{\lambda}{2d} \leq 1 \tag{2.4}$$

This relation gives the condition $\lambda \leq$ 2d which must be satisfied for Bragg scattering.

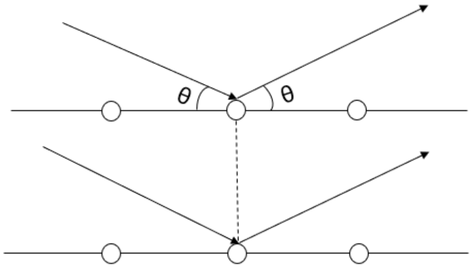

Figure 2.6: Light scattering from lattice structure

X-Ray is an electromagnetic wave, so it has an electric field component. The electric field exerts a force on charged particles. The charged particles, i.e. electrons, feel the force eE where e is the charge of electron and E is the magnitude of electric field. This force oscillates the electrons. The oscillated charged particles emits electromagnetic radiation [40]. The incident wave and the emitted wave has exactly the same frequency, so the occured phenomena can be considered as scattering. Lattice structure has a planar geometry. The waves which are scattered from the atoms in the same plane have the same phase, so these waves interfere constructively. Thanks to this constructive interference, XRD measurement yields peaks.

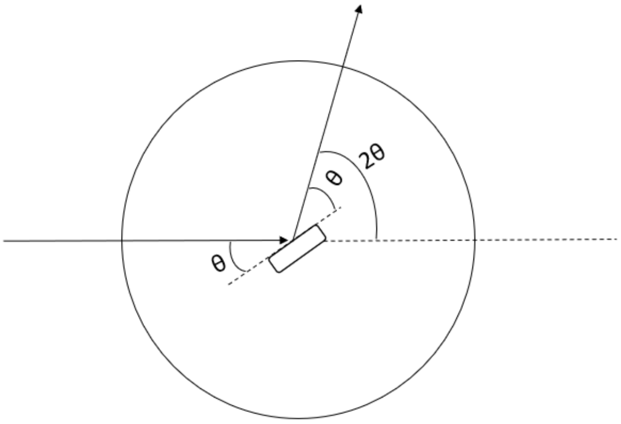

Figure 2.7: The angle of incident and scattered light in XRD measurement

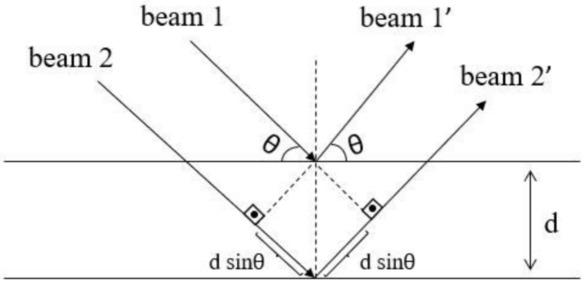

Figure 2.8: The X-Ray diffraction

In three dimensional coordinate system, lattice planes are represented by three indices which are named as Miller indices. For an orthorhombic structure,

$$\frac{1}{d_{hkl}^2} = \frac{h^2}{a^2} + \frac{k^2}{b^2} + \frac{l^2}{c^2} \tag{2.5}$$

where h, k, l are Miller indices and a, b,c are lattice parameters.

2.5.1.2 Energy Dispersive X-Ray Analysis (EDAX)

Besides the electron scattering, the incident electon beam results in emitting X-rays as it is shown in figure above. In the atomic structure, there exist electrons in the shells. Due to the incident electron beam, some of the electrons are removed from their positions. This process is called ionization. These electrons leave holes and these holes are filled by the electrons from the outer shells. The shall to shall transition of electrons result in X-ray emission. The emitted X-ray has some characteristic properties depending on the atomic number of the sample. Therefore, it is called the characteristic X-ray. An apparatus attached on the SEM set up can detect these characteristic X-rays. Therefore, the atomic ratio of different atoms in sample are obtained from their characteristic X-rays.

2.5.1.3 Scanning Electron Microscopy (SEM)

When an electron beam illuminates the sample, luminascence and scattering take place because of the electron-matter interactions. Either luminascence or scattering of electrons supply information about the structure. For instance, the electrons scattered from surface allow to determine the surface morphology.

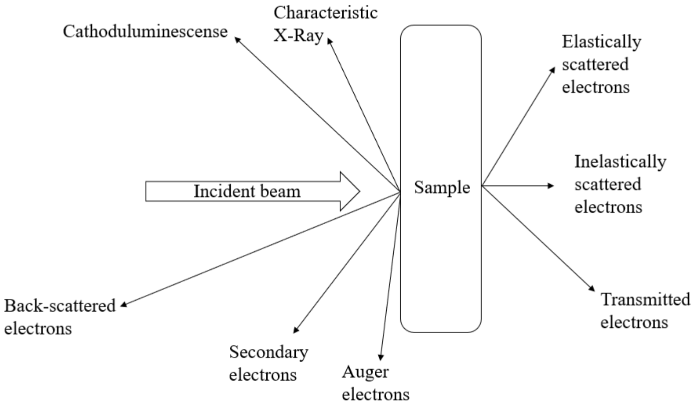

Figure 2.9: The emitted electrons and waves from sample under electron beam bombardment

Detecting both backscattered and secondary electrons underlie the SEM imaging. When the incident electron beam hits the sample, some of the electrons are reflected as a result of the elastic interactions. These electrons are called backscattered electrons [41]. The energies of backscattered electrons are bigger than 50 eV [42]. Backscattered electrons contribute to imaging the surface in which they are reflected. The incident (primary) electrons excite the electrons of the sample. Because of this excitation, some electrons are scattered from the sample. These electrons are called secondary electrons. The energies of secondary electorns must be less than 50 eV to say ‘secondary’ [43]. Since secondary electrons scattered from the surface of the sample, they are detected to analyze the topography of surface in SEM [44].

2.5.1.4 Atomic Force Microscopy (AFM)

AFM is a tip-based method to describe the topography of the surface. The AFM set up consist of a laser diode, detector, cantilever, tip and a piezoelectric holder. Because the tip is a tiny and brittle apparatus, keeping the tip fixed and moving the sample to scan the surface is logical. Thanks to the piezoelectric holder, the sample can be moved in three dimensions in nanometric precision [45, 46].

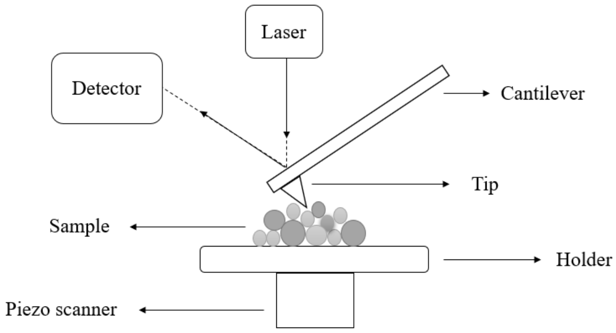

Figure 2.10: The representation of atomic force microscopy

The cantilever is bended by the attractive and repulsive forces, exerted by the charges of the sample, on tip. Therefore, the cantilever can be considered as a spring which oscillates due to the exerting forces. The spring force is given by Hooke's law.

$$F = -k\Delta x \tag{2.6}$$

The force F may differ depending on whether the tip is touching the sample or not (i.e. if touch, the friction force exist, if not attractive force dominates) and Δx supplies the topographical information [45, 46].

2.5.1.5 Raman Spectroscopy

Raman spectroscopy is a powerful way of characterization in which the vibrational modes of a sample are analyzed. The molecules in lattice makes oscillatory motion and oscillations in each directions are denoted by vibrational modes. In Raman spectroscopy, the sample is illuminated by a laser light with known frequency. The laser light scatters from the molecules inelastically and the scattered light is detected by a CCD detector. Since the Raman effect depends on the interaction of light and the molecules of sample, Raman spectroscopy results in outcomes which are specific for the materials what the sample contains. Hence, the outcome of Raman spectroscopy can be considered as a fingerprint of a material.

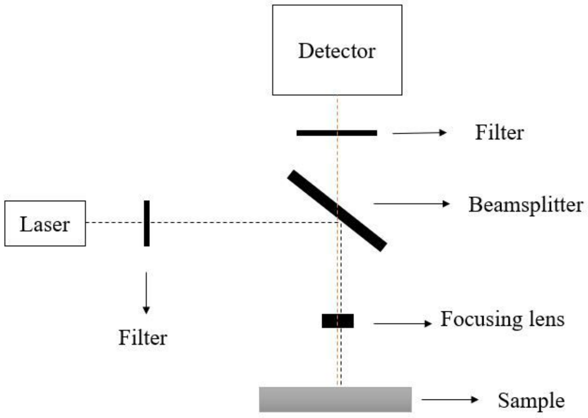

Figure 2.11: The representation of Raman spectroscopy

2.5.2 Optical Characterization Methods

To measure the optical properties of materials such as real and imaginary parts of the refractive index, absorption coefficient and optical band gap, there are specifically designed experimental set-ups and various spectroscopy techniques. UV-Vis spectroscopy and ellipsometry are two most popular optical characterization methods given in this part.

2.5.2.1 UV-Visible Spectroscopy

UV-Vis spectroscopy is a technique to determine both direct and indirect energy band gap. When the light beam is sent to a sample, some portion of the incident light is absorbed and some other portions are reflected and transmitted.

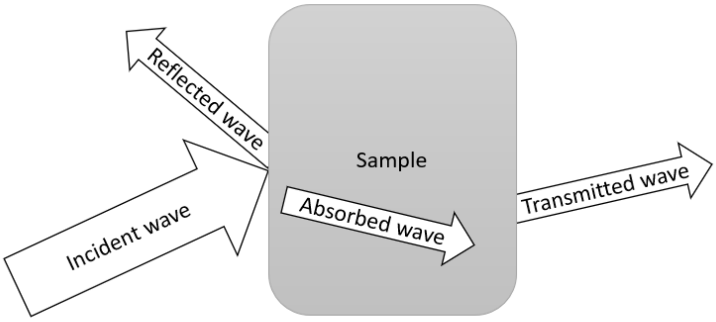

Figure 2.12: The absorption, reflection and transmission of incident beam

UV-Vis spectroscopy based on the absorption of ultraviolet or visible light by sample. The light which proceed into the crystal attenuated, so its amplitude decraeses and then it is completely absorbed. The absorption coefficient represents the attenuation of light in structure.

Absorption coefficient is formulated as:

$$\alpha = -\frac{1}{t} ln \frac{1-R}{T} \tag{2.7}$$

where is the absorption coefficient, t is the thickness of sample, R is reflectance and T is the transmittance [47]. For the case in which R is neglectable, the absorption coefficient is formulated as:

$$\alpha = \frac{1}{t} ln \frac{1}{T} \tag{2.8}$$

Therefore, absorption coefficient can be calculated if the thickness of crystal structure and the transmittance is known. Transmittance is the ratio of the intensities of transmitted and incident waves. UV-Vis spectroscopy measures the transmittance, so it allows to calculate the absorption coefficient. As it is stated in reference [48], the absorption coefficient (α) and energy of photon ($h\nu$) obey the following relation.

$$(\alpha h\nu) = A[h\nu - E_g \pm E_p]^n \tag{2.9}$$

where A is a constant, E_g is the energy gap and E_p is the energy of phonon. For the allowed transitions, n is equal to 1/2 and 2 for direct and indirect transitions respectively. For the forbidden transitions, n is equal to 3/2 and 3 for direct and indirect transitions respectively [48]. Therefore, for the allowed transitions, $(\alpha h\nu)^2$ vs $h\nu$ graph results in the direct band gap and $(\alpha h\nu)^{\frac{1}{2}}$ vs $h\nu$ graph results in the indirect band gap of semiconductors.

2.5.2.2 Spectroscopic Ellipsometry

Ellipsometry is a technique to reveal either the optical constants or thicknesses of the materials by analyzing the refracted or transmitted light. It is a fast and contactless measurement technique which do not cause any damage on samples [49]. In ellipsometry, a light source send a polarized beam on the sample. After the light is reflecting from the sample, its polarization changes owing to some factors such as scattering, backside reflection and inhomogenous thickness of sample [49]. Ellipsometry measures the amplitude ratio ψ and the phase difference Δ between the s-polarized and p-polarized light to evaluate the polarization change [49].

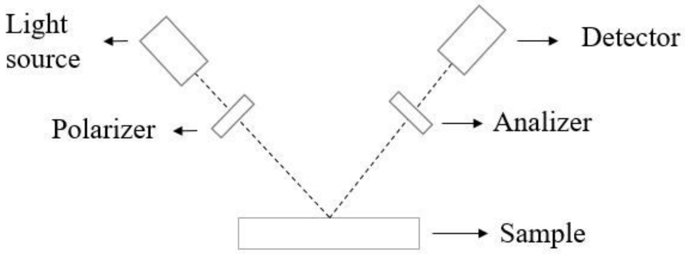

Figure 2.13: The schematic representation of spectroscopic ellipsometry

Changing wavelength results in a spectra in spectroscopic ellipsometry measurement. There are many theoretical models (i.e, Drude model, Cody-Lorentz model etc.) to evaluate the measured values. The fitting of measured values into the proper model supplies real and imaginary parts of the refractive index and dielectric function, thickness, absorption coefficient and surface roughness of samples [49] .

2.5.3 Electrical Characterization Methods

2.5.3.1 *I-V* Measurement

Two probe method and four probe method are common ways to determine the *I-V* characteristics of samples. Although four probes are more difficult to integrate, four probe method supplies the data which is more easy to interpret [50]. In contrast to two probe method, the wires that voltage is measured and current is supplied are different in four probe method as it is shown in Figure 13. Even though there are two more contacts and the wire and contact resistances still exist, the voltage impedence guarantees to eliminate the voltage drop in four probe method [50]. Therefore, four probe method is usually preferred to calculate the resistivity from *I-V* measurements.

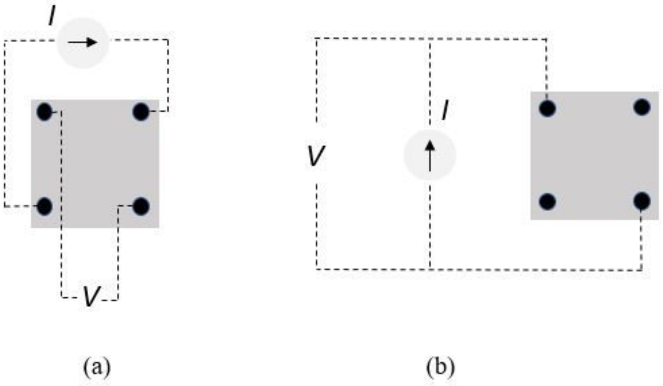

Figure 2.14: Two probe and four probe measurement

The resistivity of arbitrarily shaped samples is measured by the small contacts located at the corners of the sample if the sample has a uniform thickness [50]. The masks with a van der Pauw geometry provides such contacts. The parameters such as size, thickness and temperature of the sample affects the resistivity [50]. The contributions of these parameters are included by correction factors. Then, the resistivity and sheet resistance are formulated as:

$$\rho = \frac{\pi t}{ln2}(\frac{V}{I}) \tag{2.10}$$

$$R_s = \frac{\rho}{t} = \frac{\pi}{ln2}\frac{V}{I} \tag{2.11}$$

where t is the thickness of a sample [51].

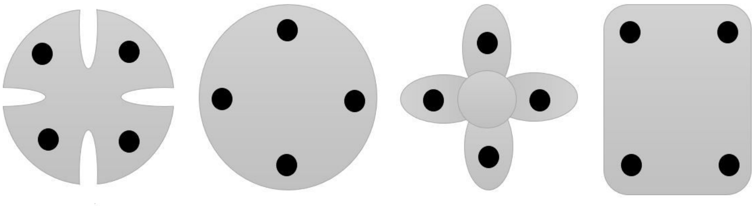

Figure 2.15: Some mask shapes

2.5.3.2 Photoconductivity

Photoconductivity is basically the increment of electrical conductivity owing to absorbing light [52]. The conductivity of a sample is low in dark. When the sample is illuminated by a light having a sufficient energy to overcome the atomic bonds, the free electrons and free holes are created. These free charges are transported along the sample by recombination. Thus, such a motion of charge carriers increases the conductivity.

The dark conductivity of a sample is given by

$$\sigma = e(n\mu_n + p\mu_p) \tag{2.12}$$

where μn and μp are the mobilities n and p are the number of negative and positive charge carries per unit volume [53]. In the illuminated case, there is additional $\Delta\sigma$ part, so the conductivity becomes

$$\sigma + \Delta\sigma = e(n\mu_n + p\mu_p) + e(\Delta n\mu_n + \Delta p\mu_p) = e[\mu_n(n + \Delta n) + \mu_p(p + \Delta p)] \tag{2.13}$$

Furthermore, the conductivity allows to calculate the activation energy. Arrhenius equation describes the rate constant and activation energy over a temperature interval. The Arrhenius equation is:

$$\sigma = Ae^{\frac{-E_a}{k_b T}} \tag{2.14}$$

where A, E_a , k_b and T are pre-exponential factor, activation energy, Boltzman's constant and temperature respectively [47]. Therefore, the slope of $ln\sigma$ vs $\frac{1}{T}$ graph gives the activation energy.

CHAPTER 3

EXPERIMENTAL TECHNIQUES AND DETAILS

3.1 Introduction

In this chapter, experimental details of the Bridgman growth of SnSbSe crystal, the deposition of SnSbSe thin films and structural, optical and electrical characterization of both crystal and thin films are introduced. At the beginning, the crystal growth is examined. The detais in either sintering or sealing process processes and the parameters in Bridgman process are investigated. Then, the deposition of SnSbSe thin films are evaluated by giving the details of sample preparation and thermal evaporation processes. The deails of heat treatment process such as temprature and duration are also introduced. Then, the experimental techniques for the characterization of SnSbSe crystal and SnSbSe thin films are given. For the structural characterization, XRD, SEM, EDAX, AFM and Raman measurements are performed. Furthermore, Spectroscopic Ellipsometry and UV-Vis Spectroscopy measurements carried out for the optical and either *I*-*V* measurement or temperature dependent photoconductivity measurement carried out for the electrical characterization. The schematic representations of the tools used in experiments and the details of measurements are investigated as well.

3.2 Growth of SnSbSe Crystal

3.2.1 Sintering Process

Sintering is basically melting the elements in a crucible to make a homogeneously mixed ingot. In this study, $SnSbSe_2$ crystal structure is planned to grow, so the desired molar ratio of elements is 1:1:2. To obtain this molar ratio, 2.22 g Sn, 2.24 g Sb and 2.88 g Se pellets were sensitively weighed. In order to clean the quartz crucible, a crucible was filled with distilled water, acetone, isopropanol and a dilute HF solution; and it was ultrasonically vibrated for 5, 15, 15 and 1 minutes respectively. Then, the inner surface of quartz crucible is coated with carbon to prevent any interactions with the quartz crucible and the growing crystal structure. The crucible was filled with the pellets and then it was vacuumed up to 10^{-5} Torr. After vacuuming, the crucible was sealed with an oxy-acetylene flame and it was located in a sintering furnace. Then, the heating process started at room temperature and the temperature was increased 150 °C per each hour until reaching 850 °C. After sintering at 850 °C for 25 hours, the sintering furnace was turned off and the crucible was left in a furnace for spontaneous cooling until reaching the room temperature. Thus, the mixture of molten pellets solidify and the sintering process results in an amorphous $SnSbSe_2$ ingot.

3.2.2 Bridgman Process

The Bridgman process takes place in a vertical Bridgman furnace which has three temperature zones and a crucible can move in a furnace through these zones. For starting Bridgman growth, a crucible which is sintered in previous step is located in a holder and temperatures of the upper, middle and lower zones were set as 850 °C, 500 °C, 400 °C respectively. After settings, the crucible starts to move from upper to the lower zone with the speed 2 mm/h. The temperature difference between zones guarantees that pellets molten in hot zones solidify in colder zones and create a solid structure. Solidification of melt on this structure during Bridgman process result in a crystal growth. Therefore, the motion of crucible through zones yields a crystal structure.

Figure 3.1: The sintering process of amorphous $SnSbSe_2$ ingot

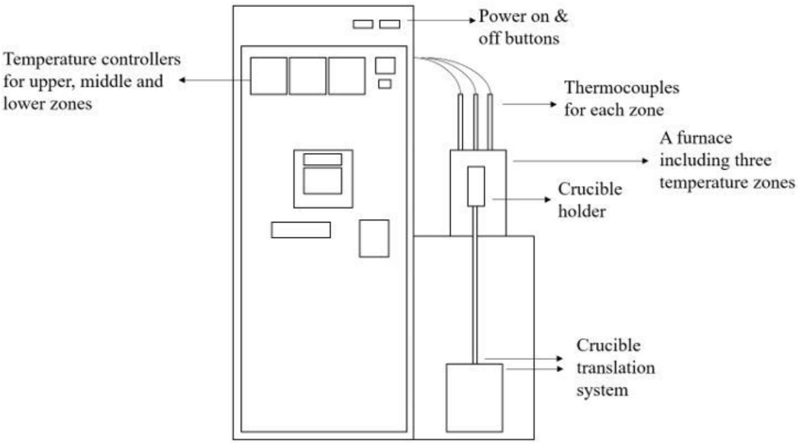

Figure 3.2: The schematic representation and picture of vertical Bridgman system

3.3 Thin Film Deposition

3.3.1 Sample Preparation

SnSbSe thin films were deposited on glass substrates. Before deposition, 2x2 and 2x1 cm soda-lime glass substrates were cleaned in detergent solution, acetone, alcohol and hydrogen-per-oxide solution by ultrasound vibration. After cleaning, each substrates were dried by nitrogen gas to remove any droplets. Then, silicon masks which have van der Pauw geometry were attached on the 2x1 cm substrates to make contacts for the electrical measurements. Finally, all substrates were stuck on a holder.

3.3.2 Thermal Evaporation

A piece of previously grown SnSbSe crystal was crushed in order to be used as a powder in thermal evaporation. 1 gram of powder was put into the degassed boat and the holder containing all substrates were located in a chamber. Then, the chamber were vacuumed until 10^{-5} Torr and the deposition carried out on the substrates at room temperature by keeping the deposition rate as minimum as possible to deposite the thin layer in a much controlled manner. After the deposition, 0.8 g of powder had been left in a boat.

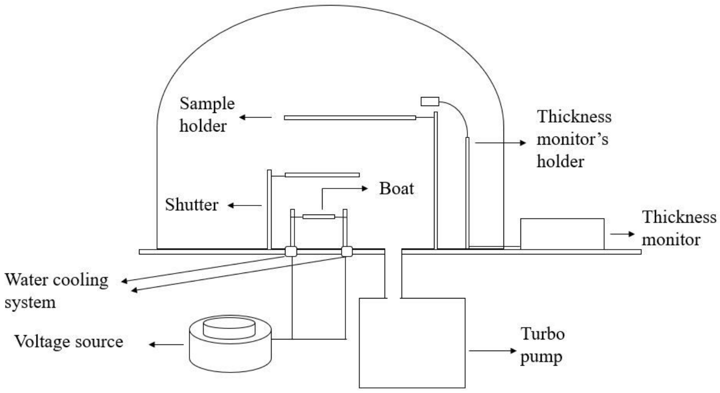

Figure 3.3: The schematic representation of thermal evaporation system

3.3.3 Thickness Measurement

After the thin film deposition, thicknesses of the deposited layers were measured by DEKTAK profilometer. The thickness were measured from different points of samples to control whether the thickness is uniform all over the film surface or not. As a result, the film thickness was measured as 250 nm and it was almost uniform through film surface.

3.3.4 Heat Treatment

In order to observe the effect of annealing on the structural, optical and electrical properties of SnSbSe thin films; one sample was kept as 'as grown' and the others were annealed at 100 °C, 200 °C, 300 °C and 400 °C for 30 minutes. The annealing process carried out in nitrogen environment to prevent oxidation.

3.4 Characterization of SnSbSe Crystal and SnSbSe Thin Films

3.4.1 Structural Characterization

3.4.1.1 XRD Measurement

To show the crystallinity and calculate the structural paramaters such as interplanar distance, dislocation density, stress and strain, XRD measurement of bulk crystal carried out by using Rigaku Miniflex Diffractometer (Cu: $K\alpha, \lambda$ = 1.54 Å) in 0 to 90 degree interval. The measurement was performed with the scan speed 4 degree per second. Then, the bulk crystal pestled to make a crystal powder and the XRD measurement of a SnSbSe powder performed in the same conditions.

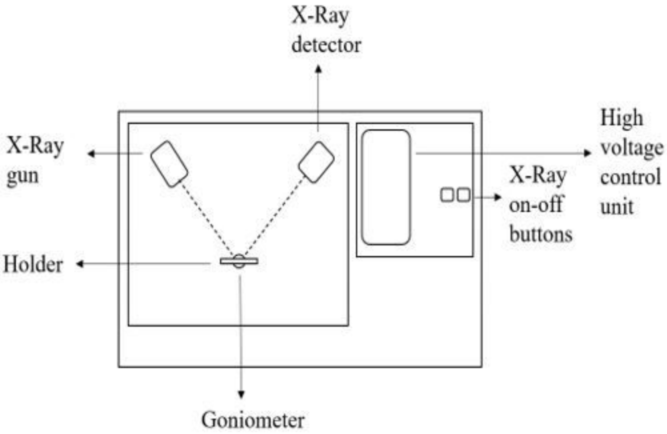

Figure 3.4: The schematic representation of Rigaku X-Ray Diffractometer

Moreover, the XRD measurement of both as drown and annealed SnSbSe thin films was performed in 10 – 90 degree interval with scan speed 4 degree per second. These measurements allow not only calculating the structural parameters but also observing the effect of annealing on crystal structure.

3.4.1.2 SEM Measurement

The surface and lateral sides of SnSbSe bulk crystal and the surfaces of as grown and annealed SnSbSe thin films were scanned by ZEISS evo 15 scanning electron microscope.

3.4.1.3 EDAX Measurement

The characteristic X-rays belong to Sn, Sb and Se elements which were radiated during SEM masurements of SnSbSe bulk crystal and SnSbSe thin films were detected by an EDX detector. Therefore, the weight and atomic percentages of each elements in either bulk crystal or as grown and annealed thin films were determined.

3.4.1.4 AFM Measurement

The surface morphologies of as grown and annealed SnSbSe thin films were investigated by Veeco MultiMode V atomic force microscope. The maximum and average values of heights and depths in certain selected areas on film's surface were reported.

3.4.1.5 Raman Measurement

Raman measurement of SnSbSe bulk crystal was carried out by Horiba-Jobin Yvon i550 whose laser has a wavelength 532 nm. Furthermore, the Raman spectra of either as grown or annealed SnSbSe thin films were measured to observe how Raman modes are affected by annealing temperature.

3.4.2 Optical Characterization

3.4.2.1 Spectroscopic Ellipsometry

The real and imaginary parts of either refractive index (n and k) or dielectric constant (ϵ_1 and ϵ_2) of SnSbSe bulk crystal were measured by GES5E Sobra variable angle ellipsometry device. Moreover, energy band gap of a bulk crystal was obtained by fitting the Cody-Lorentz model to the measured values.

3.4.2.2 UV-Visible Spectroscopy

Transmissions of SnSbSe thin films as a function of wavelength in 300-1100 nm interval were measured by Perkin Elmer Lambda 45 UV-Vis spectrometer in order to calculate the absorption coefficient for obtaining the energy band gap using Tauc plots.

3.4.3 Electrical Characterization

3.4.3.1 *I-V* Measurement

The four corners of SnSbSe bulk crystal was coated by In to create ohmic contacts and copper wires were properly attached on these contacts via silver paste. Then, the current vs voltage (*I-V*) relation of the bulk crystal was measured by Keithley 2400 sourcemeter in ± 4 V interval in dark environment. Furthermore, the measurement was repeated under the illumination of halogen lamp to observe the *I-V* behaviour of Sample under light. The *I-V* behaviour of as grown and annealed SnSbSe thin films were investigated by the same set up as well.

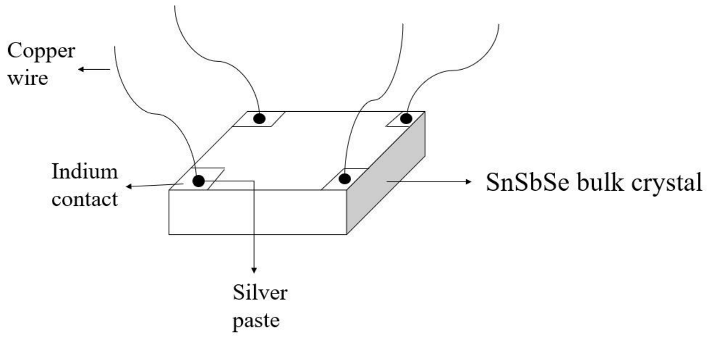

Figure 3.5: The In contacts on SnSbSe bulk crystal

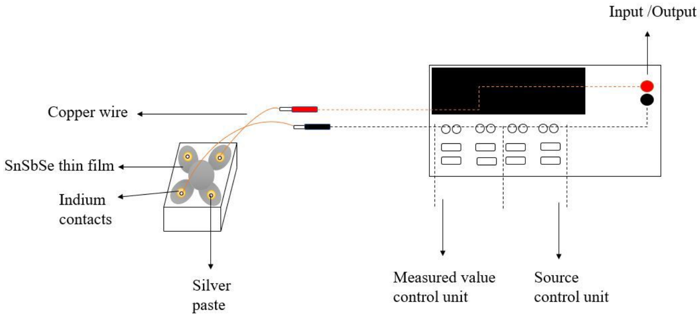

Figure 3.6: The schematic representation of *I*-*V* measurement set up

3.4.3.2 Temperature Dependent Photoconductivity

Both as grown and annealed SnSbSe thin films were placed in a Janis VPF cryostat. The *I*-*V* measurent was performed in 100-320 °K interval by increasing the temperature 10 °K at each step by using Lake-Shore 331 temperature controller device. At each step, the *I*-*V* relation of SnSbSe thin films were firstly measured by Keithley 619 electrometer in dark medium. Then, 50, 60, 70, 80, 90 mA current was supplied to halogen lamp in a cryostat by Keithley 220 current source. These current values resulted in a light with intensities 20, 35, 55, 80, 100 mW/cm^{-2} and the same measurement was repeated under these lights.

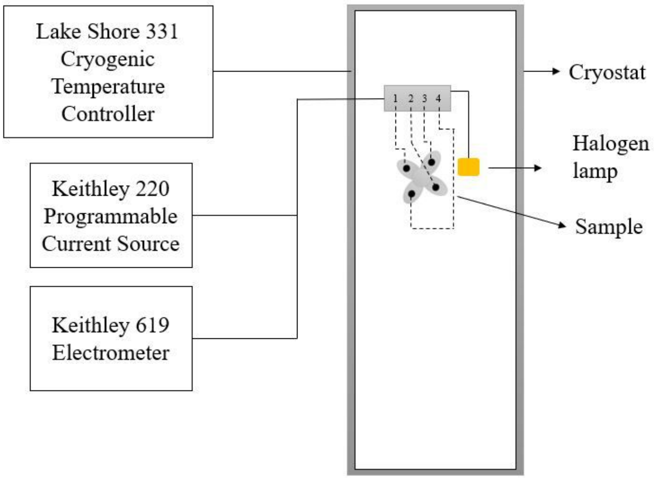

Figure 3.7: The schematic representation of cryostat

CHAPTER 4

RESULTS AND DISCUSSION

4.1 Introduction

In this chapter, the structural, optical and electrical characterization of SnSbSe bulk crystal and SnSbSe thin films are introduced.

Fistly, the bulk SnSbSe is characterized. The stoichiometry and SEM images of a crystal are given and two-dimensional structure appeared in SEM images are discussed. The crystal structure is analzed by XRD and inteplanar distance, stress, strain and dislocation density of the crystal are calculated. The Raman peaks belong to the crystal structure is given as well. For the optical characterization, either the energy band gap or real and imaginary parts of refractive index measured by spectroscopic ellipsometry are evaluated. Then, the electrical conduction mechanism of SnSbSe crystal is discussed via the current vs voltage measurement.

Secondly, SnSbSe thin films are charaterized. To determine the effect of annealing tempearture on the physical properties of SnSbSe thin films, one sample is kept as 'as grown' and the others are annealed at 100 °C, 200 °C, 300 °C, 400 °C for 30 minutes. The stoichiometries of all these samples are given by EDAX measurement and the effect of annealing is discussed. The SEM images and XRD results of thin films are investigated. Also, the AFM images of thin films are given to interpret the topology of thin film's surfaces and the Raman modes are analyzed. The energy band gaps of all thin film samples determined by UV-Vis spectroscopy are introduced and the effect of annealing on band gap is discussed. The temperature dependent photoconductivity measurement of thin films are evaluated. Lastly, the conductivities and activation energies are calculated.

4.2 Characterization of SnSbSe Bulk Crystal

4.2.1 Characterization of Structural Properties

4.2.1.1 EDX Analysis

EDX analysis yields the atomic and weight percentages of constituents in SnSbSe crystal structure. In case elements may not be uniformly distributed through the crystal, several pieces clipped from different parts of the grown crystal and EDX analysis of all these pieces carried out. All these measurement indicate the stoichiometry given in Table 4.1.

Figure 4-1 shows the outcome of EDX measurement of SnSbSe crystal. In this figure, there exist only characteristic X-ray peaks of Sn, Sb and Se elements and no contributions from other elements appear. This shows the purity of the grown crystal. The unnamed peaks in Figure 4.1 might be the satellite peaks of Sn and Sb elements.

The desired stoichiometric ratio of elements for SnSbSe crystal is 1:1:2. However, Table 4.1 shows that the ratio of weight and atomic percentages of Sn, Sb and Se elements are not exactly 1:1:2. The sintering process may bring about the deviation in stoichiometry. In sintering process, the elements are molten to mix them uniformly. The melting point of Sb (904 °K) is much bigger than the melting points of Sn (505 °K) and Se (494 °K). Therefore, Sn and Se pellets are molten earlier than Sb pellets. Until Sb pellets reach the melting point, Sn and Se have already been molten so they have more time to mix each other and create bonds. These possible bonds among Sn and Se molecules may prevent the Sb atoms to hold on crystal structure. This viewpoint explains the rareness of Sb in crystal's stoichiometry. Similar stoichiometry deviations during sintering and Bridgman growth are given elsewhere [54, 55].

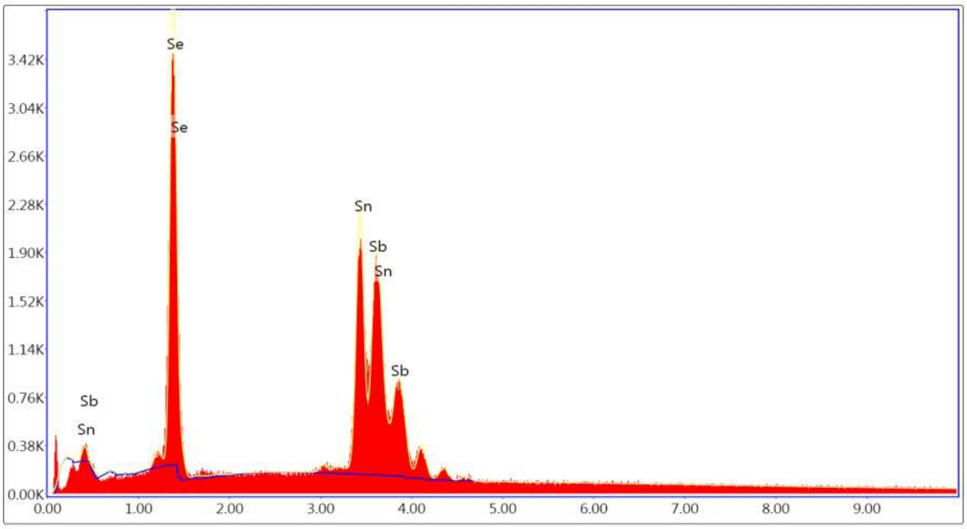

Figure 4.1: EDX spectra of SnSbSe crystal

Table 4.1: Stoichiometry of SnSbSe crystal

Elements	**Weight Percentages**	**Atomic Percentages**
Sn	30.46	24.69
Sb	22.01	17.39
Se	47.54	57.92

4.2.1.2 SEM Analysis

Figure 4-2 represents the SEM images of surface and lateral side of SnSbSe crystal. The surface of the crystal seems to be very smooth and no cracks appear. Moreover, this figure clearly shows two dimensional (2-D) layer structure of SnSbSe crystal. The literature points out that SnSe crystal has 2-D layer stucture unlike SbSe crystal [56]. Therefore, 2-D layer structure of these material may be associated with Sn-Se bonds and the observed 2-D layer characteristic of the grown SnSbSe crystal may be attributed to the relatively higher amount of Sn and lower amount of Sb as it is given in Table 4.1.

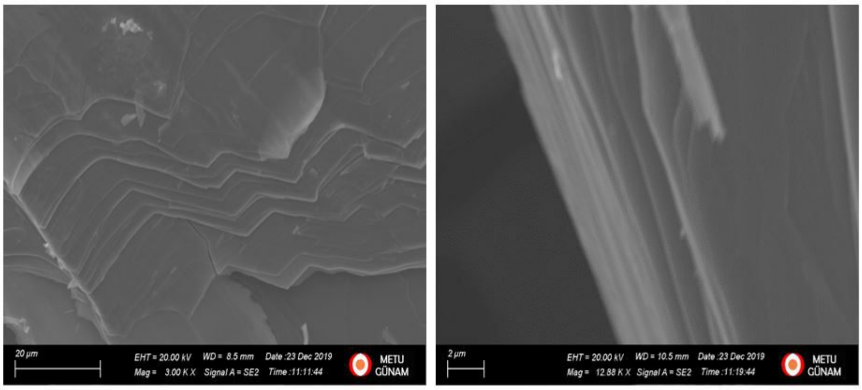

Figure 4.2: SEM of SnSbSe crystal

The atomic bonds and layer structure are related as well. The atoms make covalent bonds with the atoms within the same layer and weak van der Waals bonds with the atoms in another layer [56, 57]. This directional bonding of atoms in SnSbSe crystal may lead to anisotropic conduction mechanism and this mechanism probably be useful for device applications [58].

4.2.1.3 XRD Analysis

XRD analysis is performed to determine the orientation of the grown crystal and calculate the structural parameters such as interplanar distance, dislocation density and strain. For this purpose, the positions of diffraction peaks are compared to ICDD /Card No: 01-077-1672 and Card No: 32-1382 databases.

Figures 4.3 and 4.4 indicates that both sintering and Bridgman processes result in a crystal structure. These measurements are performed in 10 to 90 degree interval. The sharp and intense diffraction peak in Figure 4.3 shows that the SnSbSe structure is well crystalized. In the XRD graph of SnSbSe crystal, there are also really small ripples which may belong to the (011) and (400) orientations of SnSe single crystal by considering a possible shift in their positions due to the additive Sb contribution.

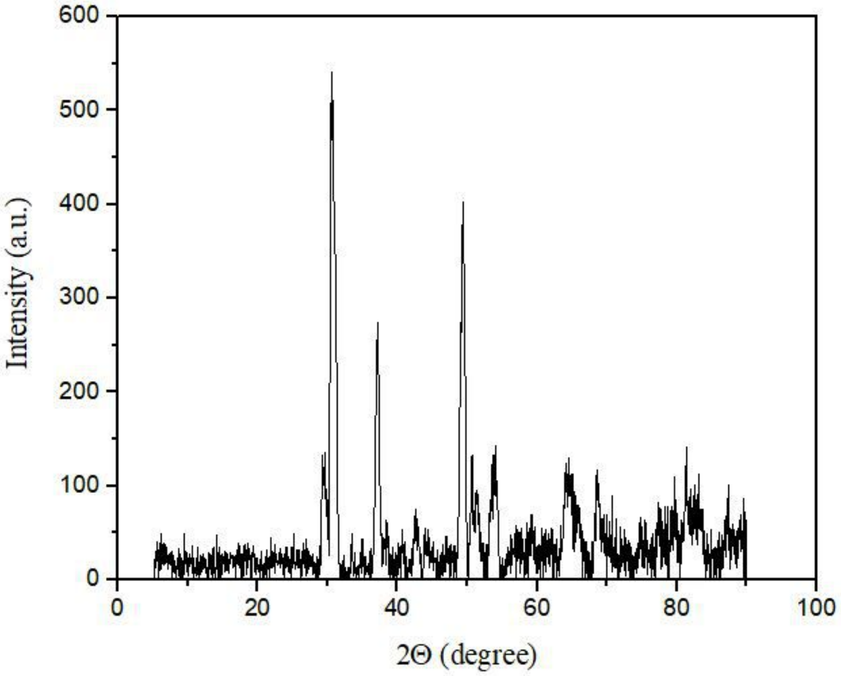

Figure 4.3: XRD graph of sintered SnSbSe powder

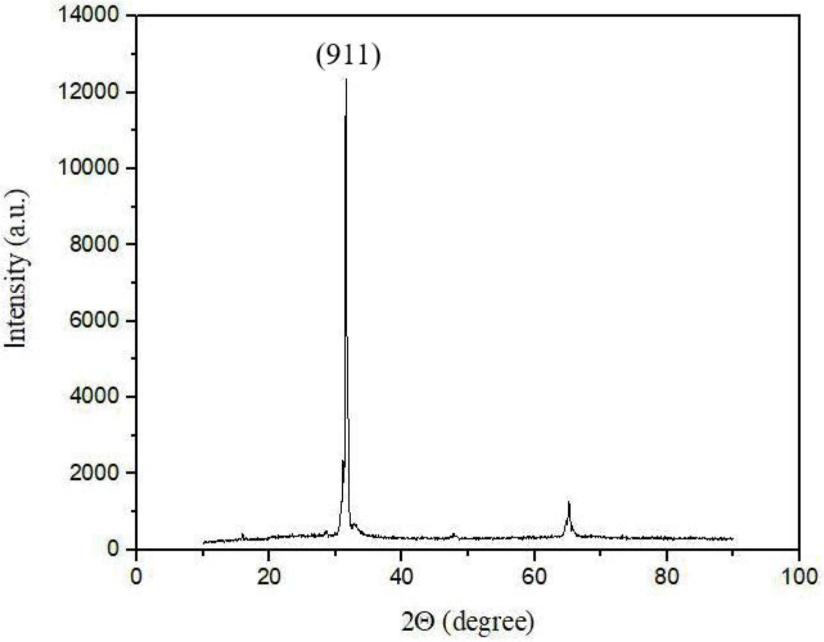

Figure 4.4: XRD graph of SnSbSe crystal

According to the database Card No: 01-077-1672, SnSbSe has orthorhombic structure and the cell paramaters are a = 3.516 nm, b = 2.596 nm, c = 4.414 nm. These parameters result in the interplanar spacing d = 2.83 Å. Furthermore, the avearage grain size is calculated as 14.77 nm, dislocation density and lattice strain are calculated as 45.87 x 10^{10} cm^{-2} and 2.45 x 10^{-3} respectively by using Scherrer's formula and the relation given in ref [59, 60].

4.2.1.4 Raman Analysis

The Raman shift of SnSbSe crystal is given in Figure 4.4 in which three main peaks appear at 107, 124 and 150 cm^{-1}. In literature, there is no study which investigates the Raman peaks of SnSbSe crystal to the best of our knowledge. For this reason, the positions of Raman peaks are compared to the positions of SnSe and SbSe Raman peaks in literature. This comparison points out that the peak at 107 cm^{-1} belongs to the B_{3g} vibration mode of SnSe crystal [61]. The peaks at 124 and 150 cm^{-1} may belong to A_g vibration mode of SnSe crystal [62]. The peaks at 124 and 150 cm^{-1} may also attributed to Sb-Sb or Se-Se bonds [63]. As a result, the Raman spectra of SnSbSe crystal exhibites similar vibrational modes to SnSe and SbSe crystals.

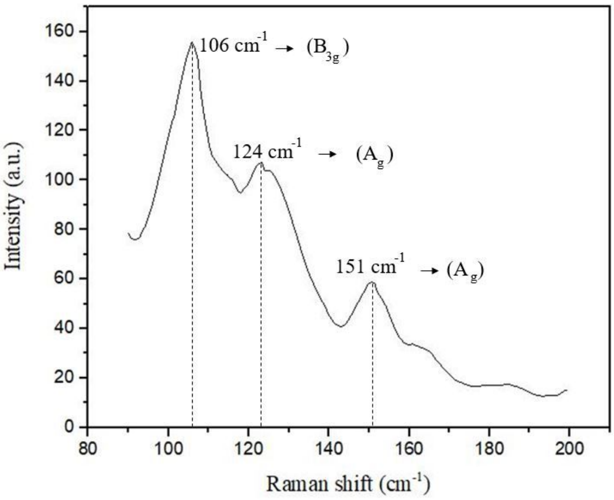

Figure 4.5: Raman spectra of SnSbSe crystal

4.2.2 Characterization of Optical Properties

The optical parameters such as the real and imaginary parts of refractive index n & k, real and imaginary parts of dielectric constant ϵ_1 & ϵ_2 and the optical band gap of SnSbSe crystal as a result of spectroscopic ellipsometry measurement are given in this part. In spectroscopic ellipsometry, the parameter related to amplitude ratio of p and s polarized light tan(ψ) and the parameter related to the phase shift between p and s polarized light cos(Δ) values are measured [49]. Also, there are many models such as Cody-Lorentz or Drude model for fitting the experimentally measured data [49]. When the values provided by a model and measured by an experiment exactly fit, the model could predict the optical properties of a material. In this study, many models were applied and the best fit was obtained in Cody-Lorentz model as it is seen in Figure 4.6.

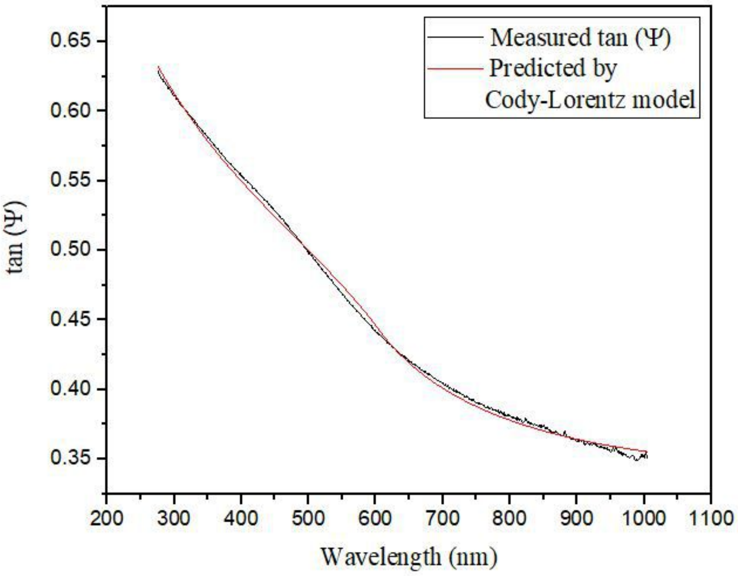

Figure 4.6: Tangent of relative amplitude vs wavelength graph of SnSbSe crystal

This model also provides the real and imaginary parts of refractive index as a function of wavelength. The spectra of these parameters are given in Figure 4.7 and Figure 4.8.

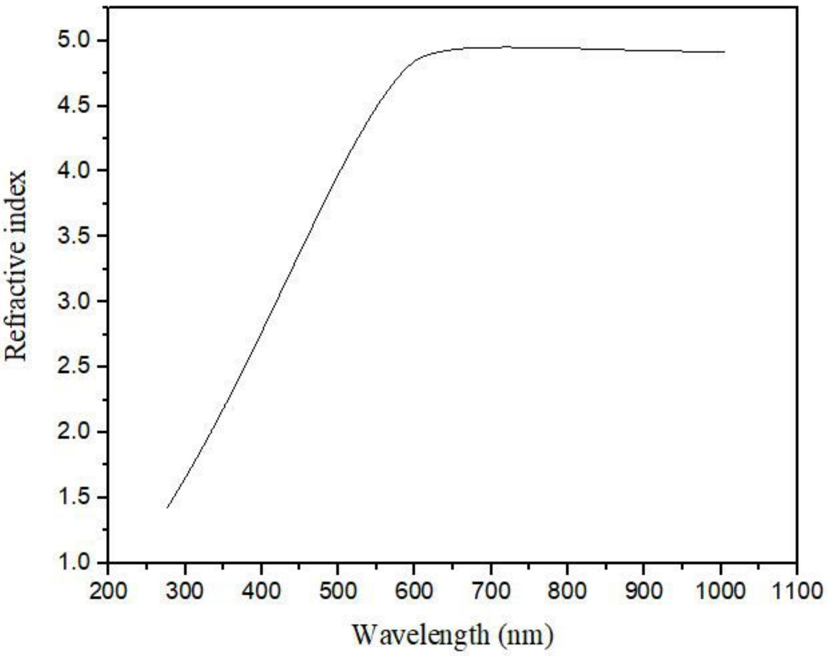

Figure 4.7: The refractive index of SnSbSe crystal as a spectrum of wavelength

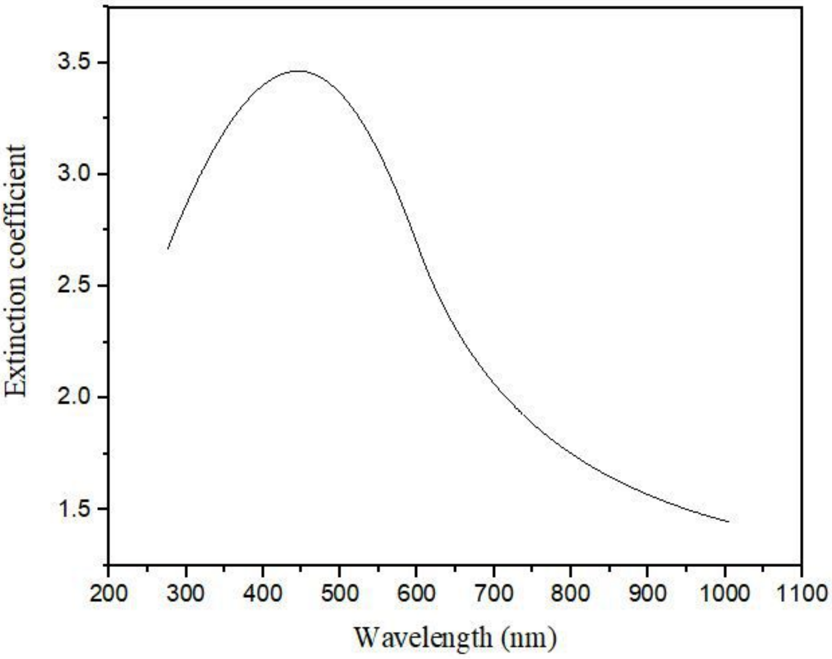

Figure 4.8: The extinction coefficient of SnSbSe crystal as a spectrum of wavelength

Figure 4.7 and Figure 8 shows that the index of refraction and the extinction coefficient is 4.91 and 2.42 respectively at 632.8 nm. Also, Cody-Lorentz model yields the optical band gap as 1.37 eV. The band gap energy of SnSbSe bulk crystal is verified by using transmission spectra which gives the band gap energy as 1.34 eV as it is given in our previous study [64]. This value is a bit larger than the direct band gap of SnSe (1.30 eV) and it is an appropriate value for photovoltaic applications [30].

4.2.3 Characterization of Electrical Properties

4.2.3.1 *I-V* Measurement

The current vs voltage *I-V* relation of SnSbSe crystal is measured from the In contacts via the attached Cu wires in both dark and illuminated environment. The dark *I-V* measurement yields a linear behaviour in ± 3.7 V interval because of the ohmic nature of In/SnSbSe interface. Moreover, the *I-V* measurement is repeated in an illuminated medium to observe the response of a crystal to light. As it is seen in Figure 4.8 (b), the slope of *I-V* graph increases when the sample is illuminated. The incident light excites the charges in valence band. The excited charges jump into the conduction band and these charges contributes to the conduction as well.

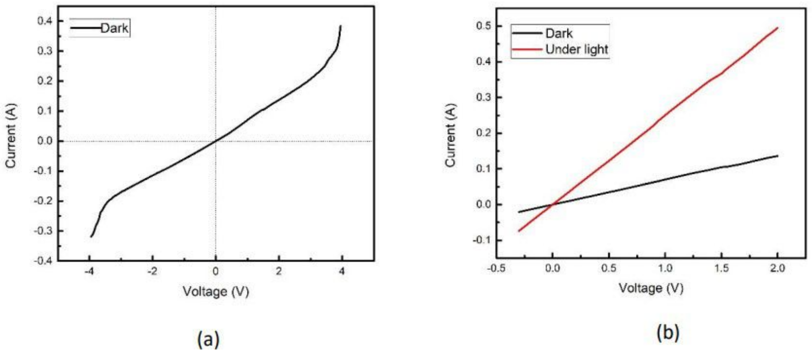

Figure 4.9: The *I-V* behaviour of SnSbSe crystal in dark medium and under light

4.3 Characterization of SnSbSe Thin Films

4.3.1 Characterization of Structural Properties

4.3.1.1 EDX Analysis

In order to examine the stoichiomery of SnSbSe thin films after deposition and the effect of annealing on the stoichiometry of thin film samples, EDX measurements of as deposited and annealed samples are given in this part. As a result of these measurements, the percentages of consituent elements are tabulated in tables below. Table 4.2 indicates that the amount of Sn in structure is lower than expected value. The possible reason of this Sn deficiency may be the formation of secondary phases [65].

Moreover, Tables 4.2, 4.3, 4.4, 4.5 and 4.6 show that the stoichiometry of SnSbSe thin films change depending on annealing temperature. As annealing temperature increases, the atomic percentage of Sn in structure increases while that of Sb decreases. The atomic percentages of Sb is also affected by annealing temperature. It increases until annealing temprature 300 ^{0}C and slightly decreases over this value. All these changes in stoichiometry of constituents in thin film structure may be explained by volatility. Among these constituents, Se is the most volatile element and its re-evaporation from substrate after deposition is well-known [66, 67]. The annealing at high temperatures may cause the re-evaporation of Se from film surface, therefore, the atomic percentages of Se decreases as annealing temperature increases. Since the given atomic percentages of constituents are relative values, a decrement in the atomic percentage of Se in structure brings about an increment in the atomic percentages of Sn and Sb relatively.

Table 4.2: Stoichiometry of as grown SnSbSe thin film

Elements	**Weight Percentages**	**Atomic Percentages**
Sn	11.18	8.43
Sb	22.89	16.83
Se	65.93	74.74

Table 4.3: Stoichiometry of SnSbSe thin film annealed at 100 °C

Elements	**Weight Percentages**	**Atomic Percentages**
Sn	14.66	11.69
Sb	33.31	25.91
Se	52.04	62.40

Table 4.4: Stoichiometry of SnSbSe thin film annealed at 200 °C

Elements	**Weight Percentages**	**Atomic Percentages**
Sn	15.76	13.02
Sb	40.35	32.49
Se	43.89	54.50

Table 4.5: Stoichiometry of SnSbSe thin film annealed at 300 °C

Elements	**Weight Percentages**	**Atomic Percentages**
Sn	20.63	17.26
Sb	38.62	31.49
Se	40.76	51.25

Table 4.6: Stoichiometry of SnSbSe thin film annealed at 400 °C

Elements	Weight Percentages	Atomic Percentages
Sn	23.83	20.09
Sb	37.28	30.64
Se	38.89	49.28

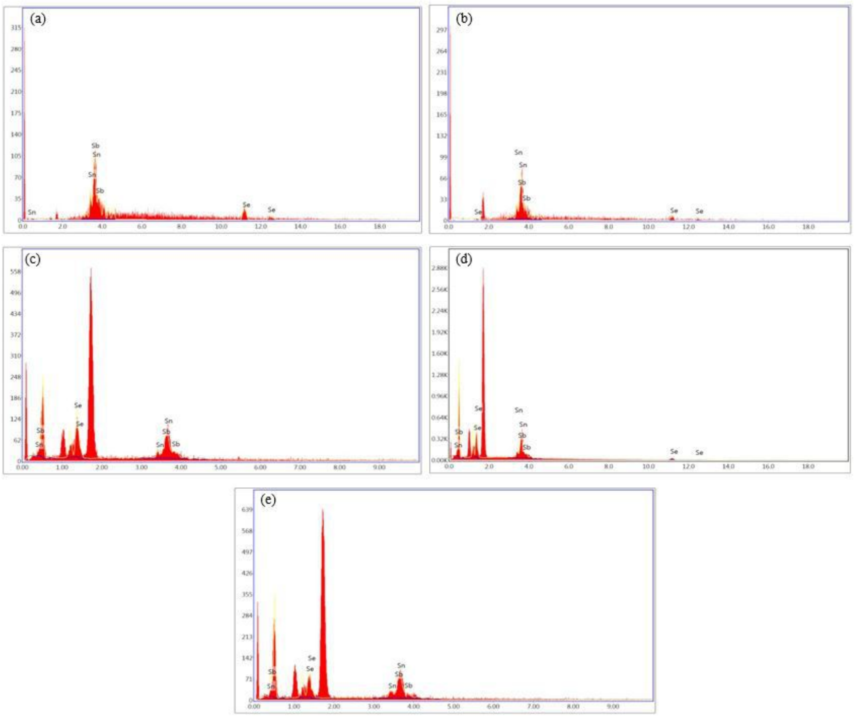

Figure 4.10: The characteristic X-Ray peaks of Sn, Sb and Se elements in SnSbSe thin films: as grown (a), annealed at 100 °C (b), annealed at 200 °C (c), annealed at 300 °C (d), annealed at 400 °C (e),

4.3.1.2 SEM Analysis

The SEM images of SnSbSe thin film are given in Figure 4.11. The images given in Figure 11-(a), (b), (c) and (d) exhibits that the film surface is smooth and no defects or cracks are observed. Therefore, it is possible to say that the annealing temperatures up to 300 °C do not cause a surface deformation. However, 400 °C is a too much value for annealing as its deformation on the film surface is clearly indicated in Figure 11-(e). Also, the grains in the surface of SnSbSe thin films are too small to observe at this magnification. This may be the possible reason of the high resistivity of these thin films.

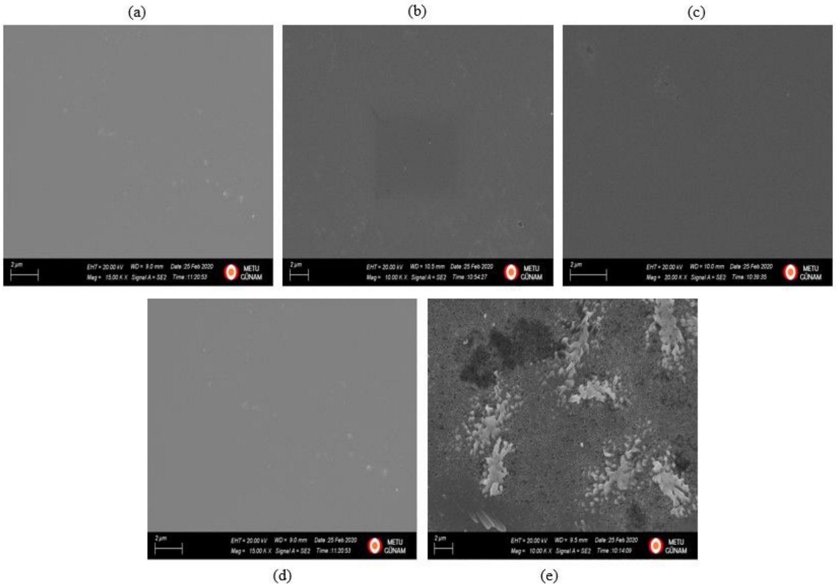

Figure 4.11: The SEM images of SnSbSe thin films: as grown (a), annealed at 100 °C (b), annealed at 200 °C (c), annealed at 300 °C (d), annealed at 400 °C (e)

4.3.1.3 XRD Analysis

The XRD measurement of as grown and annealed SnSbSe thin films performed in 10 <2Θ <90 interval the resulting XRD graphs are given in figure 4.12. In this figure, it is clearly observed that the as grown sample and the sample annealed at 100 °C are amorphous. Amorphous as grown samples are commonly obtained in depositions at low temperatures and 100 °C annealing temperature is possibly low for crystallization. The sample which is annealed at 200 °C has small peak that indicates the crystallization takes place at 200 °C annealing. The intensity of this peak increases after the annealing at 300 °C. Also, annealing at 300 °C result in another orientation (351) in crystal sturucture. The intensity of main peak decreases after annealing at 400 °C. This decrement may be attributed to the deformation on the crystal structure because of the annealing at high temperatures as it is discussed in SEM analysis.

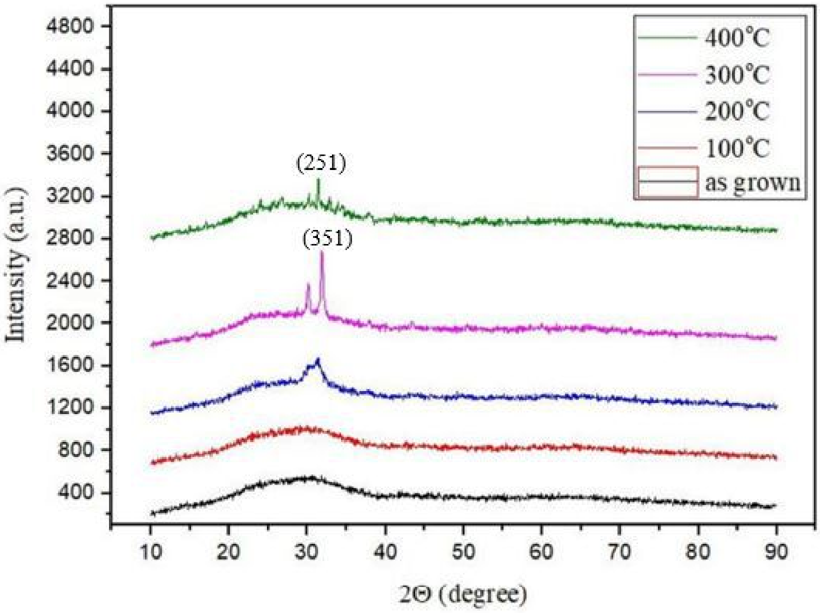

Figure 4.12: The XRD graph of as grown and annealed SnSbSe thin films

Since the samples which are annealed at 300 °C and 400 °C exhibits the crystalline structure, the structural parameters of these samples are calculated and tabulated in table 4.7.

Table 4.7: Structural parameters of SnSbSe thin films

Properties	**annealed at 300 °C**	**annealed at 400 °C**
Interplanar distance (Å)	2.77	2.85
Average grain size (nm)	35.74	49.91
Strain (x$10^{-2} lin^{-2} m^{-4}$)	10.0	7.25
Dislocation density (x$10^{10} cm^{-2}$)	7.8	4.0

The interplanar distance of the samples annealed at 300 °C and 400 °C are very close to interplanar distance of SnSbSe bulk crystal which were introduced before. Although annealing at 400 °C gives less intense peak, it is clearly seen that annealing at 400 °C results in an increment in average grain size. This implies that annealing at 400 °C makes the grain boundaries smaller. Furthermore, dislocation density decreases after annealing at 400 °C. Therefore, it can be concluded that annealing at 400 °C makes the structural parameters better. Also, full width half maximas of the peaks belong to the samples annealed at 300 °C and 400 °C are 0.26 and 0.17 respectively. The peak sharpness indicates that the sample annealed at 400 °C is well crystallized. However, the XRD peak of a sample which is annealed at 400 °C is less intense. This may also be attributed to the surface deformation of that sample since the X-Rays reflected from the film surface generates the peaks.

4.3.1.4 Raman Analysis

Figure 4.13 indicates the Raman spectrum of SnSbSe thin films. The graphs of as grown sample and the samples annealed at 200 °C and 400 °C has small ripples at 106 cm^{-1}. Similarly, the samples anneales at 100 °C and 300 °C have peaks at 106 cm^{-1}. The Raman peak at this positions also appear in the Raman spectra of SnSe and it corresponds to B_{3g} vibration mode [61]. The sample annealed at 100 °C has a ripple at 122 cm^{-1} and this peak corresponds to A_g vibration mode [62]. Moreover, the samples annealed at 200 °C and 300 °C has a peak at 156 cm^{-1}. These peaks at 156 cm^{-1} may also attributed to the A_g vibration mode of SnSe with a little shift due to the contribution of Sb [62]. Additionally, the peaks at 122 cm^{-1} and 156 cm^{-1} may represent Sb-Sb and Se-Se bonds [63]. The samples annealed at 300 ^{0}C and 400 °C has a peak at 165 cm^{-1} and a ripple at 197 cm^{-1} and these may belong to the $c(bb)\bar{c}$ vibrational mode and the vibration of Se atoms respectively [68, 69].

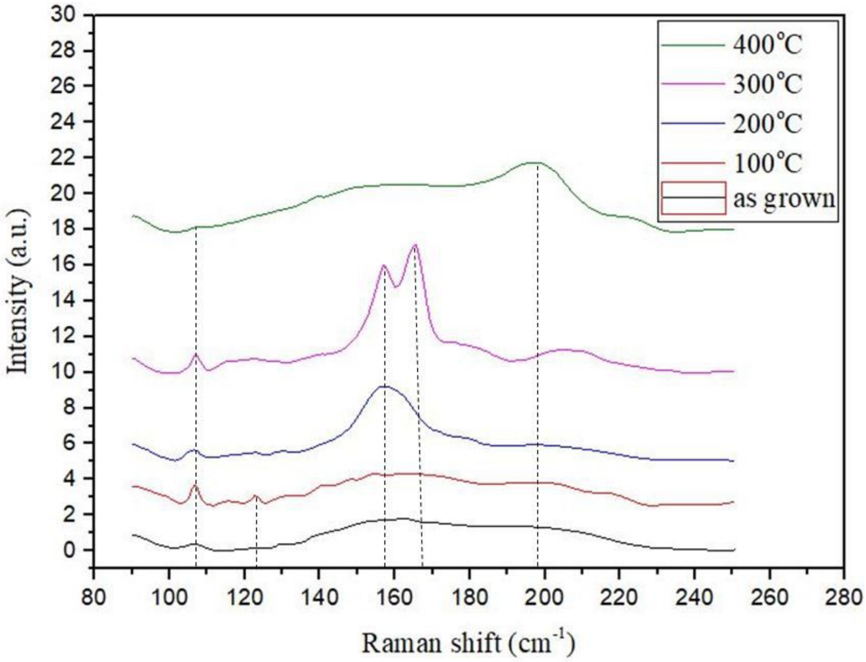

Figure 4.13: The Raman spectrum of as grown and annealed SnSbSe thin films

4.3.1.5 AFM Analysis

Atomic Force Microscopy performed for observing the topography of SnSbSe thin films. Figure 4.14 indicates the AFM images of as grown and annealed samples. The most smooth surface appears in Figure 4.14-(d) which corresponds to the sample annealed at 300 °C. This sample is also the one which shows the best crystallinity in XRD measurements. Also, the roughest surface is given in Figure 4.14-(e) which corresponds to the sample annealed at 400 °C. The surface roughness of this sample is also verified by SEM images and interpreted as the surface deformation due to high annealing temperature.

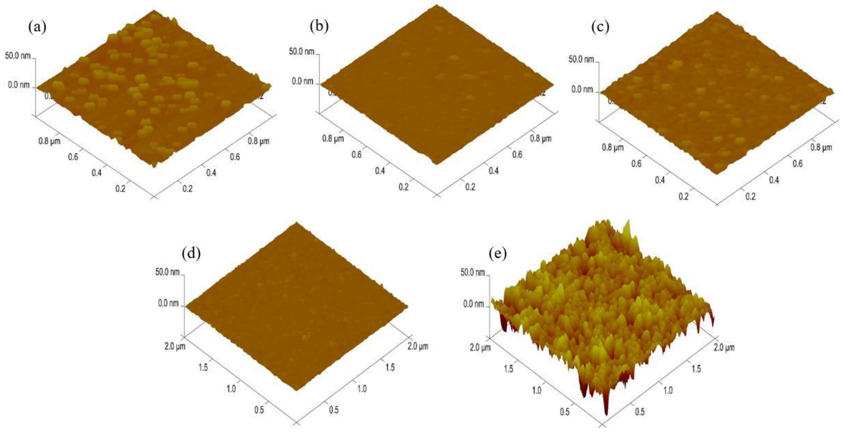

Figure 4.14: The AFM images of as grown and annealed SnSbSe thin films: as grown (a), annealed at 100 °C (b), annealed at 200 °C (c), annealed at 300 °C (d), annealed at 400 °C (e)

4.3.2 Characterization of Optical Properties

4.3.2.1 UV-Visible Spectroscopy

In this part, transmissions of as grown and annealed SnSbSe thin films are measured by UV-Visible spectroscopy and the absorption coefficients are calculated as a spectrum. Absorption coefficient of each sample are obtained at 10^4 order. As it is stated in theoretical consideration part, the linear fit in $(\alpha h\nu)^2$ vs hν graph gives the value of direct band gap while $(\alpha h\nu)^{1/2}$ vs hν graph gives the value of indirect band gap. In this study, both of these graphs are plotted and only direct band gap is observed. The high absorption coefficent indicates the direct energy band gap as well. The $(\alpha h\nu)^2$ vs hν graphs are introduced in the following figure.

The linear fits in Tauc plots carefully applied in a region at which the absorption starts. After fitting, Tauc plots given in Figure 4.15-(a), (b), (c), (d) and (e) shows that the as grown sample and the samples annealed at 100 °C, 200 °C, 300 °C and 400 °C has 1.59 eV, 1.59 eV, 1.49 eV, 1.60 eV and 1.67 eV energy band gaps respectively as tabulated in Table 4.8. The band gap of as grown sample is consistent with the band gaps of as grown SnSe and SbSe thin films [30, 31, 32]. Moreover, it is close and slighly bigger than the band gap energy of SnSbSe bulk crystal which is calculated in this study as 1.37 eV. Annealing at 200 °C causes a decrement in band gap energy. Such a narrowing in band gap energy is expected since the increasing annealing temperature yields lattice expansion and electron-phonon interaction [70, 71]. Similar observations about the annealing temperature and band gap energies could be found in refs [72, 73]. Depending on the fact that the energy band gap of as grown sample and the sample annealed at 100 °C is really close, it is possible to say that annealing 100 °C is not enough to change the structure. This argument is also supported by XRD graph which shows as grown sample and the sample annealed at 100 °C has the same structure. Annealing at 200 °C causes a considerable decrement in energy band gap and the annealing temperatures above 200 °C give rise to bigger band gap energies. A band gap widening after annealing at 300 °C and 400 °C may be explained by Burstein-Moss effect. The stoichiometric change due to annealing may cause a change in charge carrier density. The charge carriers which fill the available states may increase the band gap energy.

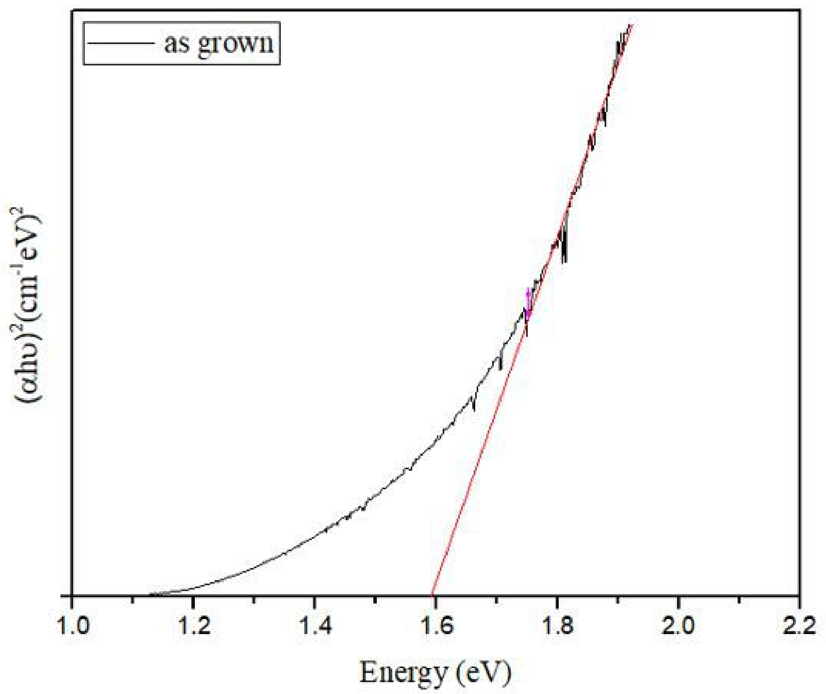

Figure 4.15: The Tauc plot of as grown sample

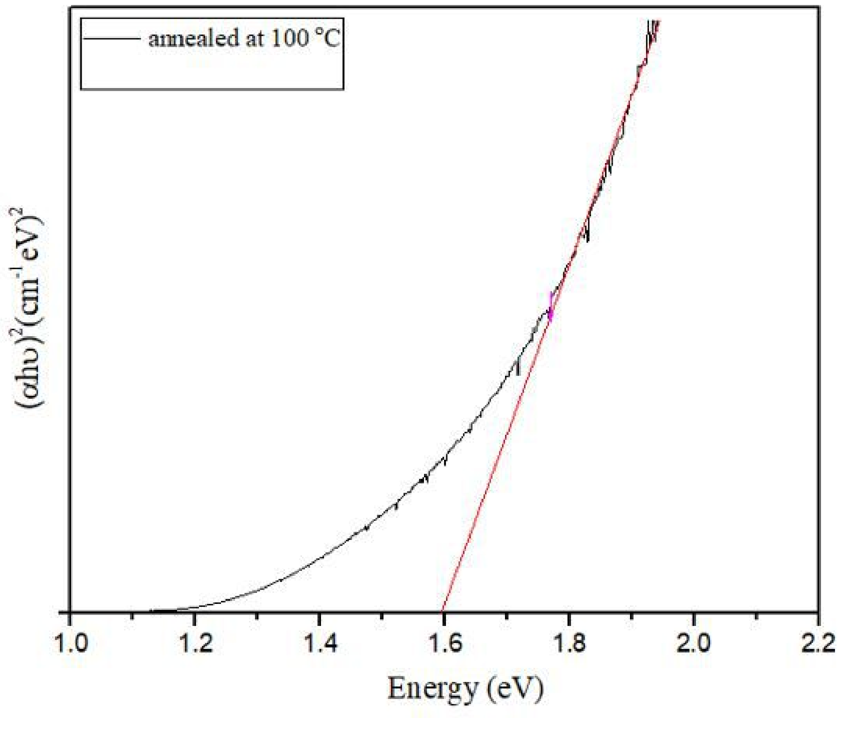

Figure 4.16: The Tauc plot of a sample annealed at 100 °C

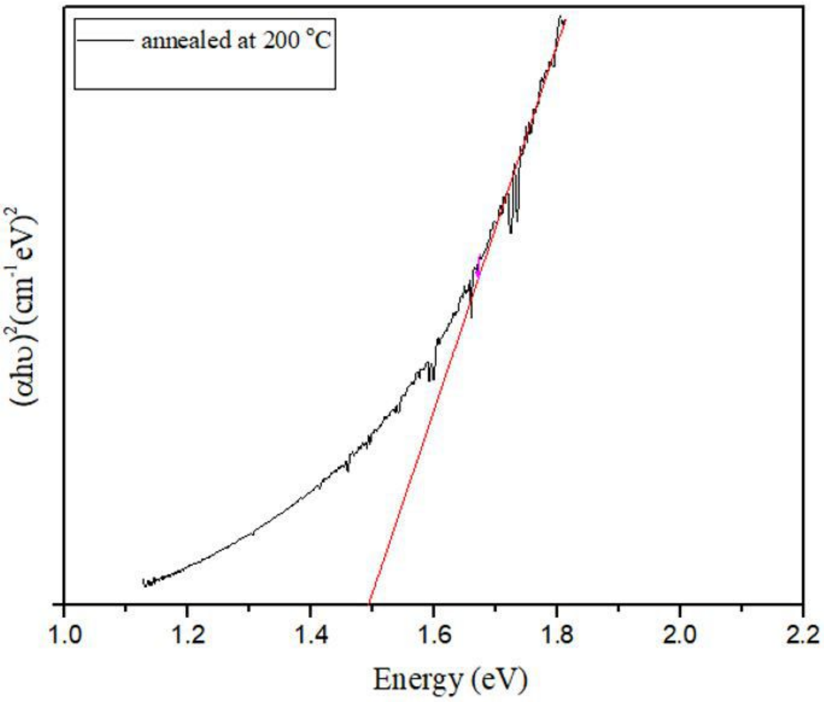

Figure 4.17: The Tauc plot of a sample annealed at 200 °C

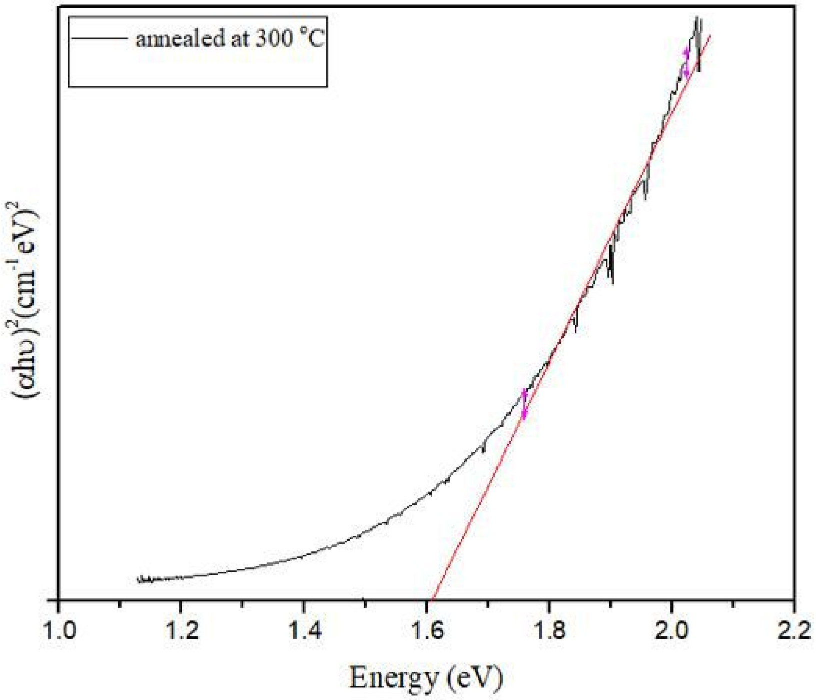

Figure 4.18: The Tauc plot of a sample annealed at 300 °C

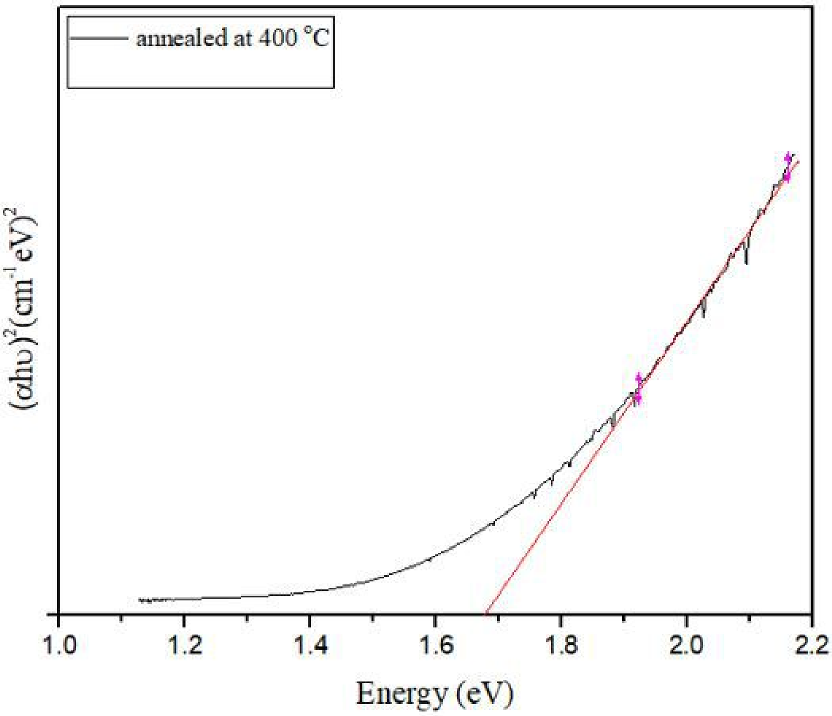

Figure 4.19: The Tauc plot of a sample annealed at 400 °C

Table 4.8: Energy band gaps of SnSbSe thin films

Samples	**Band Gap Energy (eV)**
as grown	1.59
annealed at 100 °C	1.59
annealed at 200 °C	1.49
annealed at 300 °C	1.60
annealed at 400 °C	1.67

4.3.3 Characterization of Electrical Properties

4.3.3.1 Photoconductivity Measurement

The temperature dependent photoconductivities of SnSbSe thin films are measured in dark medium and under the light with intesities 20, 35 ,55, 80, 100 mW/cm^2 in 100-300 K interval. The conductivity and activation energy of each sample are calculated. Also, these measurements allow to observe the relation between conductivity and light intensity and the relation between activation energy and annealing temperature.

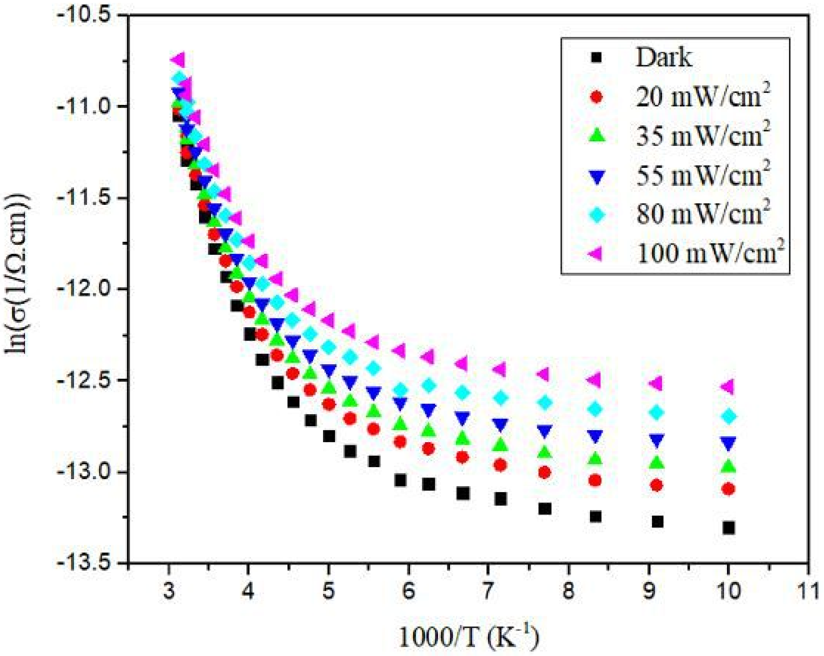

Figure 4.20: The Arrhenius plots of as grown sample

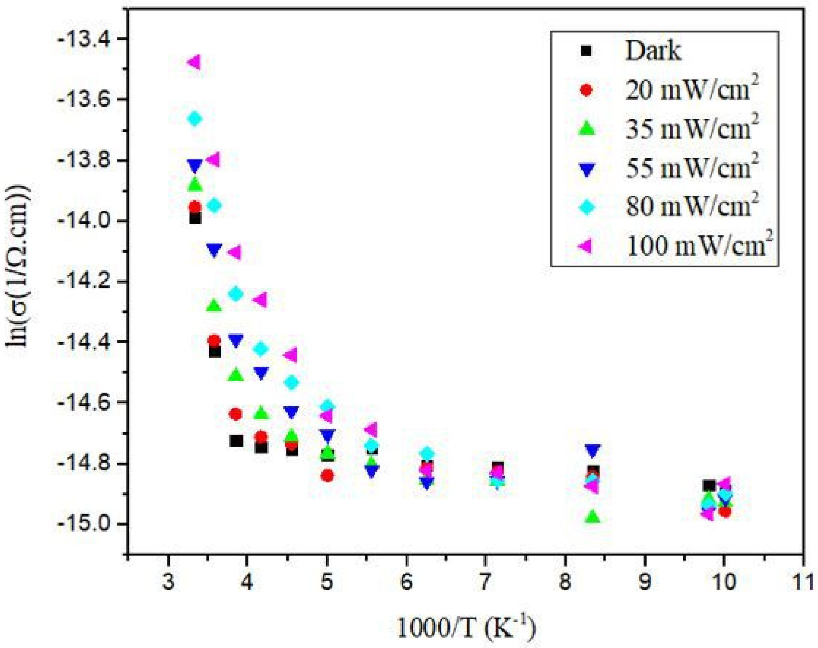

Figure 4.21: The Arrhenius plots of a sample annealed at 100 °C

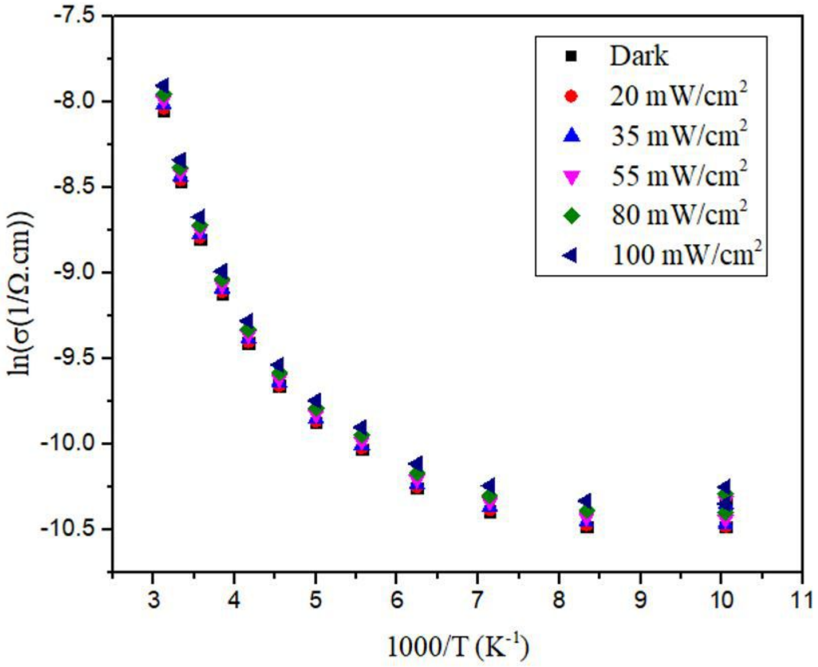

Figure 4.22: The Arrhenius plots of a sample annealed at 200 °C

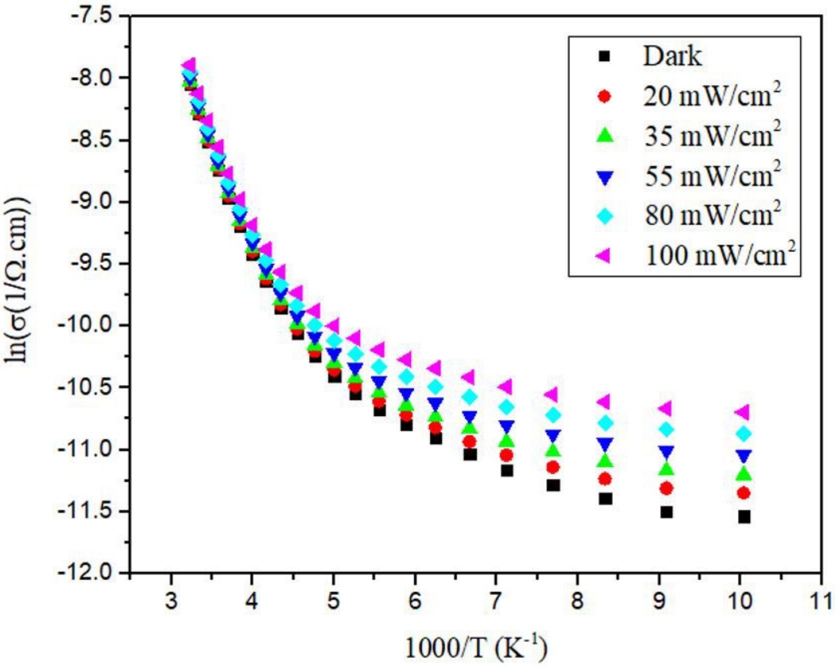

Figure 4.23: The Arrhenius plots of a sample annealed at 300 °C

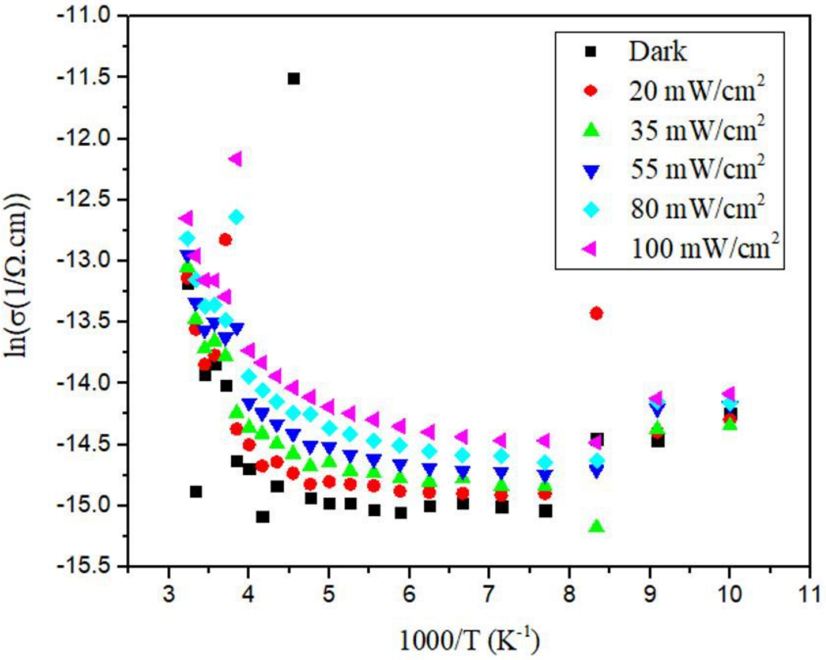

Figure 4.24: The Arrhenius plots of a sample annealed at 400 °C

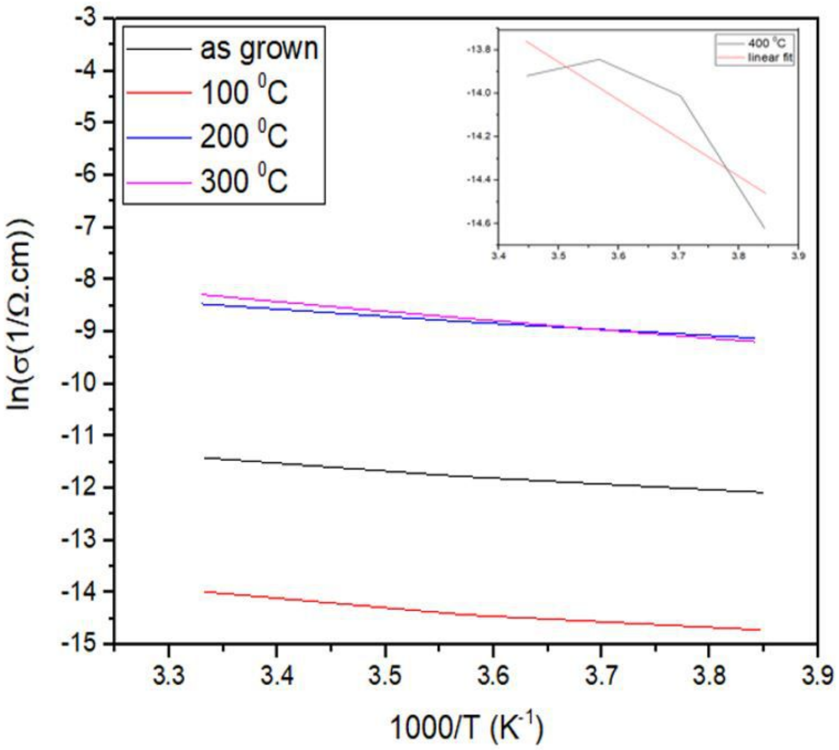

Figure 4.25: The Arrhenius plots of a samples at high energy regions

The activation energy of samples calculated using the slope of the graphs are tabulated in the following table.

Table 4.9: Activation energies of SnSbSe thin films

Samples	**Activation Energy (meV)**
as grown	106.1
annealed at 100 °C	122.3
annealed at 200 °C	126.5
annealed at 300 °C	158.7
annealed at 400 °C	151.0

The conductivities of samples as a function of temperature are given by Arrhenius equation which allows to calculate the activation energies [74].

$$\sigma(T) = \sigma_0 exp(-\frac{E_a}{kT}) \tag{4.1}$$

For electrical conduction, charge carriers must exceed the potential barriers which exist in grain boundaries. The activation energy is an energy which must be supplied to charge carriers for exceeding the potential barriers. As it is discussed in XRD analysis, the increasing annealing temperature yields bigger grain size. It also means that as annealing temperature increases the grain boundaries are being smaller. It is possible to think that smaller grain boundaries increase conductivity since charge carriers can easily be conducted from one grain to the other when the grain boundary is small. However, table 4.9 indicates that the activation energy increases when annealing temperature increases. Such an increment in activation energy implies that the increasing annealing temperature also increases the height of potential barrier between boundaries. Therefore, the charge carriers needs more energy to exceed that barrier and contribute to conduction. As it is also discussed in UV-Visible spectroscopy analysis, this effect may be attributed to the changing density of charge carriers due to the effect of annealing on the stoichiometry of samples. The change in charge carrier density may cause an increment in potential barrier height and contact resistance and these inceases the activation energy as annealing temperature increases [75]. Also, the resistivitiy of the sample annealed at 300 °C is calculated around 6.2x 10^3 Ω.cm and the p-type conductivities of samples are verified by hot probe technique.

CHAPTER 5

CONCLUSION

This study aims to growth and characterize the structural, optical and electrical properties of SnSbSe bulk crystal and SnSbSe thin films. Hence, SnSbSe bulk crystal were grown and SnSbSe thin films were deposited on glass substrates by using vertical Bridgman technique and thermal evaporation respectively. Furthermore, to investigate the effect of annealing on the physical properties, one of the thin film samples kept as ‘as grown’ and the others were annealed in nitrogen environment at 100 ^{0}C, 200 ^{0}C, 300 ^{0}C and 400 ^{0}C for 30 minutes. For the characterization of the structural properties of SnSbSe bulk crystal EDAX, SEM, XRD and Raman measurements were performed. EDAX measurement provided that the atomic ratio of elements in crystal structure as Sn: 24, Sb: 17 and Se: 57 percent. These values did not exactly match the desired stoichiometry. The possible reason of a slight deviation between the obtained and desired stoichiometries was attributed to the interactions and created bonds among elements during sintering process by taking the melting points into consideration. SEM images provided that the surface of a crystal was smooth and defect – crack free. Also, this measurement supplied two- dimensional (2-D) layer structure of SnSbSe crystal. The type of bonds among the atoms in the same layer and with the atoms in adjacent layer were determined as covalent and weak van der Waals respectively by considering the similar 2- D layer structure of SnSe single crystal. The XRD measurement gave a sharp and intense peak at around $2\Theta = 32^0$ which shows the structure was well-crystallined. By considering the positions of main peak and the orthorhombic structure of SnSbSe, the structural parameters were calculated. Raman measurement provided the peaks at 106 cm^{-1}, 124 cm^{-1} and 151 cm^{-1}. It was concluded that these peaks represent B_{3g}, A_g and A_g vibrational modes respectively. The optical characterization carried out by spectroscopic ellipsometry measurement.

The Cody-Lorentz model, whose prediciton exactly fit the experimentally measured data, provided the optical band gap as 1.37 eV, the index of refraction and extinction coeeficient as 4.9 and 2.4 at 632.8 nm respectively. Furthermore, the electrical characterization was performed by *I-V* measurement via In contacts in both dark and illuminated manner. It was observed that In/SnSbSe inteface resulted in ohmic conduction mechanism and the illumination increased the conductivity by increasing the mobility of charge carriers. Similar characterization processes were also carried out for SnSbSe thin films. The purity of deposited thin films and the change in their stoichiometry was provided by EDAX measurement. The increasing deficiency of Se in thin film structure due to the increasing annealing temperature was attributed to the re-evaporation of Se from film surface. The SEM images of as grown and annealed samples were compared and the relation between grain size and amount of resistivity was discussed. Also, the surface deformation due to the annealing at 400 °C was clearly shown. In XRD measurement, the crystalline parameters of the samples which shows the crystal structure were exhibited and the effect of annealing temperature of these parameters were discussed. The Raman peaks at 106 cm^{-1}, 122 cm^{-1}, 156 cm^{-1}, 165 cm^{-1} and 197 cm^{-1} were evaluated and the vibrational modes corrisponding to the peaks at these positions were introduced. Moreover, the surface roughness of each samples were investigated by AFM measurement and the deformation on the film surface due to the annealing at 400 °C was verified. In UV-Visible spectroscopy analysis, the absorption coefficient was given as 10^4cm^{-1} and the direct band gap of as grown sample and the samples annealed at 100 °C, 200 °C, 300 °C and 400 °C were determined as 1.59, 1.59, 1.49, 1.60 and 1.67 eV respectively. The effect of annealing temperature on the band gap energy was investigated. Lastly, p-type conductivities were observed, the activation energies of SnSbSe thin films were calculated from Arrhenius plots and the effect of annealing temperature on the activation energies was discussed.

REFERENCES

[1] C. Wolfram, O. Shelef, and P. Gertler, “How will energy demand develop in the developing world?,” *Journal of Economic Perspectives*, vol. 26, no. 1, pp. 119–38, 2012.

[2] F. Sher, O. Curnick, and M. T. Azizan, “Sustainable conversion of renewable energy sources,” 2021.

[3] S. Jabeen, S. Malik, S. Khan, N. Khan, M. I. Qureshi, and M. S. M. Saad, “A comparative systematic literature review and bibliometric analysis on sustainability of renewable energy sources,” *International Journal of Energy Economics and Policy*, vol. 11, no. 1, p. 270, 2021.

[4] I. Sarbu and C. Sebarchievici, “Solar radiation,” in *Solar Heating and Cooling Systems*, pp. 13–28, Elsevier, 2017.

[5] S. Tippireddy, P. K. DS, S. Das, and R. C. Mallik, “Oxychalcogenides as thermoelectric materials: An overview,” *ACS Applied Energy Materials*, vol. 4, no. 3, pp. 2022–2040, 2021.

[6] D. De Maio, C. D’Alessandro, A. Caldarelli, D. De Luca, E. Di Gennaro, R. Russo, and M. Musto, “A selective solar absorber for unconcentrated solar thermal panels,” *Energies*, vol. 14, no. 4, p. 900, 2021.

[7] F. Juan, Y. Wu, B. Shi, M. Wang, M. Wang, F. Xu, J. Jia, H. Wei, T. Yang, and B. Cao, “Plasmonic au nanooctahedrons enhance light harvesting and photocarrier extraction in perovskite solar cell,” *ACS Applied Energy Materials*, vol. 4, no. 4, pp. 3201–3209, 2021.

[8] A. Vijayan and N. Sandhyarani, “Synthesis and characterization of photocatalytic materials,” *Photocatalysis*, p. 1, 2021.

[9] “IX. the action of light on selenium,” *Philosophical Transactions of the Royal Society of London*, vol. 167, pp. 313–349, Dec. 1877.

[10] L. C. Wei and J. H. F. Chau, “Photoelectrochemical water splitting process using titanium dioxide photocatalyst: A brief overview,” *Malaysian Catalysis-An International Journal*, vol. 1, pp. 26–35, 2021.

[11] S. Sharma, K. K. Jain, A. Sharma, *et al.*, “Solar cells: in research and applications—a review,” *Materials Sciences and Applications*, vol. 6, no. 12, p. 1145, 2015.

[12] D. E. Carlson, “Amorphous silicon solar cells,” *IEEE Transactions on Electron Devices*, vol. 24, no. 4, pp. 449–453, 1977.

[13] A. Salavei, D. Menossi, F. Piccinelli, A. Kumar, G. Mariotto, M. Barbato, M. Meneghini, G. Meneghesso, S. Di Mare, E. Artegiani, *et al.*, “Comparison of high efficiency flexible cdte solar cells on different substrates at low temperature deposition,” *Solar Energy*, vol. 139, pp. 13–18, 2016.

[14] Y. Nagoya, K. Kushiya, M. Tachiyuki, and O. Yamase, “Role of incorporated sulfur into the surface of cu (inga) se2 thin-film absorber,” *Solar energy materials and solar cells*, vol. 67, no. 1-4, pp. 247–253, 2001.

[15] M. Pagliaro, G. Palmisano, and R. Ciriminna, *Flexible solar cells.* Wiley-VCH, 2008.

[16] K. Chopra, P. Paulson, and V. Dutta, “Thin-film solar cells: an overview,” *Progress in Photovoltaics: Research and applications*, vol. 12, no. 2-3, pp. 69–92, 2004.

[17] G. Beaucarne, “Silicon thin-film solar cells,” *Advances in OptoElectronics*, vol. 2007, 2007.

[18] E. Artegiani, A. Gasparotto, P. Punathil, V. Kumar, M. Barbato, M. Meneghini, G. Meneghesso, F. Piccinelli, and A. Romeo, “A new method for cdsexte1-x band grading for high efficiency thin-absorber cdte solar cells,” *Solar Energy Materials and Solar Cells*, vol. 226, p. 111081, 2021.

[19] M. Kaelin, D. Rudmann, and A. Tiwari, “Low cost processing of cigs thin film solar cells,” *Solar Energy*, vol. 77, no. 6, pp. 749–756, 2004.

[20] D. Sell and H. Casey Jr, “Optical absorption and photoluminescence studies of thin gaas layers in gaas–al x ga1- x as double heterostructures,” *Journal of Applied Physics*, vol. 45, no. 2, pp. 800–807, 1974.

[21] N. Shinde, D. Dubal, D. Dhawale, C. Lokhande, J. Kim, and J. Moon, “Room temperature novel chemical synthesis of cu2znsns4 (czts) absorbing layer for photovoltaic application,” *Materials Research Bulletin*, vol. 47, no. 2, pp. 302–307, 2012.

[22] F. Meinardi, S. Ehrenberg, L. Dhamo, F. Carulli, M. Mauri, F. Bruni, R. Simonutti, U. Kortshagen, and S. Brovelli, “Highly efficient luminescent solar concentrators based on earth-abundant indirect-bandgap silicon quantum dots,” *Nature Photonics*, vol. 11, no. 3, pp. 177–185, 2017.

[23] A. Catalano, R. Daiello, J. Dresner, B. Faughnan, A. Firester, J. Kane, H. Schade, Z. Smith, G. Swartz, and A. Triano, “Attainment of 10 percent conversion efficiency in amorphous silicon solar cells,” in *16th Photovoltaic Specialists Conference*, p. 1421, 1982.

[24] R. M. Swanson, “Approaching the 29% limit efficiency of silicon solar cells,” in *Conference Record of the Thirty-first IEEE Photovoltaic Specialists Conference, 2005.*, pp. 889–894, IEEE, 2005.

[25] M. Imamzai, M. Aghaei, Y. H. M. Thayoob, and M. Forouzanfar, “A review on comparison between traditional silicon solar cells and thin-film cdte solar cells,” in *Proceedings of National Graduate Conference (Nat-Grad*, pp. 1–5, 2012.

[26] S. Dias, S. Chirakkara, N. Patel, and S. Krupanidhi, “Gallium and indium co-doped zno as a transparent conducting oxide for cu 2 sns 3 photodetectors,” *Journal of Materials Science: Materials in Electronics*, vol. 29, no. 3, pp. 2131–2139, 2018.

[27] M. A. Sattar, N. Al Bouzieh, M. Benkraouda, and N. Amrane, “First-principles study of the structural, optoelectronic and thermophysical properties of the π-snse for thermoelectric applications,” *Beilstein journal of nanotechnology*, vol. 12, no. 1, pp. 1101–1114, 2021.

[28] Q. Han, Y. Zhu, X. Wang, and W. Ding, "Room temperature growth of snse nanorods from aqueous solution," *Journal of materials science*, vol. 39, no. 14, pp. 4643–4646, 2004.

[29] Z. Zhang, X. Zhao, and J. Li, "Snse/carbon nanocomposite synthesized by high energy ball milling as an anode material for sodium-ion and lithium-ion batteries," *Electrochimica Acta*, vol. 176, pp. 1296–1301, 2015.

[30] W. J. Baumgardner, J. J. Choi, Y.-F. Lim, and T. Hanrath, "Snse nanocrystals: synthesis, structure, optical properties, and surface chemistry," *Journal of the American Chemical Society*, vol. 132, no. 28, pp. 9519–9521, 2010.

[31] K. Kutorasinski, B. Wiendlocha, S. Kaprzyk, and J. Tobola, "Electronic structure and thermoelectric properties of n-and p-type snse from first-principles calculations," *Physical Review B*, vol. 91, no. 20, p. 205201, 2015.

[32] Y. Yu, R. Wang, Q. Chen, and L.-M. Peng, "High-quality ultralong sb2se3 and sb2s3 nanoribbons on a large scale via a simple chemical route," *The Journal of Physical Chemistry B*, vol. 110, no. 27, pp. 13415–13419, 2006.

[33] R. Vadapoo, S. Krishnan, H. Yilmaz, and C. Marin, "Electronic structure of antimony selenide (sb2se3) from gw calculations," *physica status solidi (b)*, vol. 248, no. 3, pp. 700–705, 2011.

[34] S. S. Zumdahl and D. J. DeCoste, *Chemical principles*. Cengage Learning, 2012.

[35] G. Parker, *Introductory semiconductor device physics*. CRC Press, 2004.

[36] V. Tran, R. Soklaski, Y. Liang, and L. Yang, "Layer-controlled band gap and anisotropic excitons in few-layer black phosphorus," *Physical Review B*, vol. 89, no. 23, p. 235319, 2014.

[37] W. Dumke, "Two-phonon indirect transitions and lattice scattering in si," *Physical Review*, vol. 118, no. 4, p. 938, 1960.

[38] R. P. Mooney, S. McFadden, Z. Gabalcová, and J. Lapin, "An experimental–numerical method for estimating heat transfer in a bridgman furnace," *Applied Thermal Engineering*, vol. 67, no. 1-2, pp. 61–71, 2014.

[39] A. Kumar, J. Banerjee, and K. Muralidhar, “Thermal modeling of crystal growth by the czochralski method including radius control.,” *Journal of Scientific and Industrial Research*, vol. 61, no. 8, pp. 607–616, 2002.

[40] B. D. Cullity, *Elements of X-ray Diffraction*. Addison-Wesley Publishing, 1956.

[41] D. Pendse and A. Chin, “Cathodoluminescence and transmission cathodoluminescence,” 2001.

[42] J. Kirschner, “On the influence of backscattered electrons on the lateral resolution in scanning auger microscopy,” *Applied physics*, vol. 14, no. 4, pp. 351–354, 1977.

[43] J. Scholtz, D. Dijkkamp, and R. Schmitz, “Secondary electron emission properties,” *Philips journal of research*, vol. 50, no. 3-4, pp. 375–389, 1996.

[44] H. Seiler, “Secondary electron emission in the scanning electron microscope,” *Journal of Applied Physics*, vol. 54, no. 11, pp. R1–R18, 1983.

[45] R. A. Wilson and H. A. Bullen, “Basic theory-atomic force microscopy (afm),” *Department of Chemistry, Northern Kentucky University, Highland Heights, KY*, vol. 41099, 2005.

[46] A. Vilalta-Clemente, K. Gloystein, and N. Frangis, “Principles of atomic force microscopy (afm),” *Proceedings of Physics of Advanced Materials Winter School*, 2008.

[47] D. T. Quan, “Electrical properties and optical absorption of snse evaporated thin films,” *physica status solidi (a)*, vol. 86, no. 1, pp. 421–426, 1984.

[48] D. Pathinettam Padiyan, A. Marikani, and K. Murali, “Electrical and photoelectrical properties of vacuum deposited snse thin films,” *Crystal Research and Technology: Journal of Experimental and Industrial Crystallography*, vol. 35, no. 8, pp. 949–957, 2000.

[49] K. Hinrichs and K.-J. Eichhorn, *Ellipsometry of functional organic surfaces and films*, vol. 52. Springer, 2014.

[50] D. K. Schroder, *Semiconductor material and device characterization*. John Wiley & Sons, 2015.

[51] N. Makori, I. Amatalo, P. Karimi, and W. Njoroge, “Optical and electrical properties of snse thin films for solar cell applications,” *Am. J. Condens. Matter Phys*, vol. 4, no. 5, p. 87, 2014.

[52] R. S. Quimby, *Photonics and lasers: an introduction*. John Wiley & Sons, 2006.

[53] G. Agostini and C. Lamberti, *Characterization of semiconductor heterostructures and nanostructures*. Elsevier, 2011.

[54] D. J. Kim, J.-H. Oh, H. S. Kim, Y. S. Kim, M. Jeong, C. G. Kang, W. J. Jo, H. Choi, J. G. Kim, S. H. Lee, *et al.*, “Characteristics of tlbr single crystals grown using the vertical bridgman-stockbarger method for semiconductor-based radiation detector applications,” *Materials Science Poland*, vol. 34, no. 2, pp. 297–301, 2016.

[55] U. N. Roy, O. Okobiah, G. Camarda, Y. Cui, R. Gul, A. Hossain, G. Yang, S. Egarievwe, and R. James, “Growth and characterization of detector-grade cdmnte by the vertical bridgman technique,” *AIP Advances*, vol. 8, no. 10, p. 105012, 2018.

[56] L. Li, Z. Chen, Y. Hu, X. Wang, T. Zhang, W. Chen, and Q. Wang, “Single-layer single-crystalline snse nanosheets,” *Journal of the American Chemical Society*, vol. 135, no. 4, pp. 1213–1216, 2013.

[57] L.-D. Zhao, G. Tan, S. Hao, J. He, Y. Pei, H. Chi, H. Wang, S. Gong, H. Xu, V. P. Dravid, *et al.*, “Ultrahigh power factor and thermoelectric performance in hole-doped single-crystal snse,” *Science*, vol. 351, no. 6269, pp. 141–144, 2016.

[58] H. Song, T. Li, J. Zhang, Y. Zhou, J. Luo, C. Chen, B. Yang, C. Ge, Y. Wu, and J. Tang, “Highly anisotropic sb2se3 nanosheets: gentle exfoliation from the bulk precursors possessing 1d crystal structure,” *Advanced Materials*, vol. 29, no. 29, p. 1700441, 2017.

[59] M. Terlemezoglu, Ö. B. Sürücü, T. Çolakoğlu, M. K. Abak, H. Güllü, Ç. Erçelebi, and M. Parlak, “Construction of self-assembled vertical nanoflakes on cztsse thin films,” *Materials Research Express*, vol. 6, no. 2, p. 026421, 2018.

[60] R. Rudman, “Handbook of x-rays, for diffraction, emission, absorption, and microscopy (kaelble, emmett f., ed),” 1968.

[61] P. Fernandes, M. Sousa, P. M. Salome, J. Leitão, and A. d. Da Cunha, "Thermodynamic pathway for the formation of snse and snse 2 polycrystalline thin films by selenization of metal precursors," *CrystEngComm*, vol. 15, no. 47, pp. 10278–10286, 2013.

[62] S. Zhao, H. Wang, Y. Zhou, L. Liao, Y. Jiang, X. Yang, G. Chen, M. Lin, Y. Wang, H. Peng, *et al.*, "Controlled synthesis of single-crystal snse nanoplates," *Nano research*, vol. 8, no. 1, pp. 288–295, 2015.

[63] Z. Ivanova, E. Cernoskova, V. Vassilev, and S. Boycheva, "Thermomechanical and structural characterization of gese2–sb2se3–znse glasses," *Materials Letters*, vol. 57, no. 5-6, pp. 1025–1028, 2003.

[64] T. Bektas, M. Terlemezoglu, O. Surucu, M. Isik, and M. Parlak, "Growth and optical characterization of sn0. 6sb0. 4se layer single crystals for optoelectronic applications," *Materials Science in Semiconductor Processing*, vol. 141, p. 106434, 2022.

[65] S. T. Lee, M. J. Kim, G.-G. Lee, S. G. Kim, S. Lee, W.-S. Seo, and Y. S. Lim, "Effects of sn-deficiency on thermoelectric properties of polycrystalline sn1-xse compounds," *Current Applied Physics*, vol. 17, no. 5, pp. 732–737, 2017.

[66] M. Parlak and C. Ercelebi, "The effect of substrate and post-annealing temperature on the structural and optical properties of polycrystalline inse thin films," *Thin Solid Films*, vol. 322, no. 1-2, pp. 334–339, 1998.

[67] W. Sharaman, R. Birkmire, S. Marsillac, M. Marudachalam, N. Orbey, and T. Russell, "Effect of reduced deposition temperature, time, and thickness on cu (inga) se/sub 2/films and devices," in *Conference Record of the Twenty Sixth IEEE Photovoltaic Specialists Conference-1997*, pp. 331–334, IEEE, 1997.

[68] X. Gong, H. Wu, D. Yang, B. Zhang, K. Peng, H. Zou, L. Guo, X. Lu, Y. Chai, G. Wang, *et al.*, "Temperature dependence of raman scattering in single crystal snse," *Vibrational Spectroscopy*, vol. 107, p. 103034, 2020.

[69] J. Ge, Y. Yu, and Y. Yan, "Earth-abundant orthorhombic bacu2sn (se x s1–x) 4 (x 0.83) thin film for solar energy conversion," *ACS Energy Letters*, vol. 1, no. 3, pp. 583–588, 2016.

[70] A. Franceschetti, “First-principles calculations of the temperature dependence of the band gap of si nanocrystals,” *Physical Review B*, vol. 76, no. 16, p. 161301, 2007.

[71] S. Wang, J. Ma, W. Li, J. Wang, H. Wang, H. Shen, J. Li, J. Wang, H. Luo, and D. Li, “Temperature-dependent band gap in two-dimensional perovskites: Thermal expansion interaction and electron–phonon interaction,” *The journal of physical chemistry letters*, vol. 10, no. 10, pp. 2546–2553, 2019.

[72] N. Shahzad, N. Ali, I. Haq, S. Shah, S. Ali, Q. Ahmad, F. Azlullah, A. Kalam, and A. Al-Sehemi, “Annealed tin selenide (snse) thin film material for solar cell application,” *Chalcogenide Letters*, vol. 17, no. 7, pp. 347–351, 2020.

[73] S. Rajesh, M. M. Parvathi, A. Mohan, and V. Arivazhagan, “Preparation and characterization of vacuum evaporated snse and snse2 multilayer thin films,” in *AIP Conference Proceedings*, vol. 1451, pp. 206–208, American Institute of Physics, 2012.

[74] M. Dogruer, G. Yildirim, and C. Terzioglu, “Effect of annealing temperature on magnetoresistivity, activation energy, irreversibility and upper critical field of the cu-diffused mgb 2 bulk superconductors,” *Journal of Materials Science: Materials in Electronics*, vol. 24, no. 1, pp. 392–401, 2013.

[75] V. Kumar, I. Rawal, and V. Kumar, “Fabrication of n-zno/p-si++ hetero-junction devices for hydrogen detection: effect of annealing temperature,” *Silicon*, pp. 1–13, 2021.

CURRICULUM VITAE

PERSONAL INFORMATION

Surname, Name: Bektaş, Tunç
Nationality: Turkish (TC)
Date and Place of Birth: 28 November 1994, Ankara
Marital Status: Single
Phone: +90 312 210 76 47

EDUCATION

Degree	Institution	Year of Graduation
M.S.	Physics, Middle East Technical University	Fall, 2022
B.S.	Physics, Middle East Technical University	Spring, 2019

PUBLICATIONS

Articles

Bektas T., Terlemezoglu M., Surucu O., Isik M., Parlak M., 'Growth and optical characterization of $Sn_{0.6}Sb_{0.4}Se$ layer single crystal for optoelectronic applications', Materials Science in Semiconductor Processing, 141 (2022) 106434. DOI: https://doi.org/10.1016/j.mssp.2021.106434

Oral Presentations

Bektas T., Terlemezoglu M., Surucu O., Parlak M.,'$SnSbSe_2$ Crystal: Growth by Vertical Bridgman Technique and Investigation of Its Structural, Optical and Electrical Properties', PVCON 2020 International Conference on Photovoltaic Science, 2021

Poster Presentations

Bektas T., Terlemezoglu M., Surucu O., Parlak M., 'Characterization of Thermally Evaporated $SnSbSe_2$ Thin Films', 26^{th} Condensed Matter Physics Meeting, 2021.